J. Fluid Mech., page 1 of 37.
doi:10.1017/jfm.2011.268

Pore-scale mass and reactant transport in multiphase porous media flows

A. Parmigiani[1]†, C. Huber[2], O. Bachmann[3] and B. Chopard[1]

[1] Computer Science Department, University of Geneva, CH-1227 Carouge, Switzerland

[2] School of Earth and Atmospheric Sciences, Georgia Institute of Technology, GA 30332, USA

[3] Department of Earth and Space Sciences, University of Washington, WA 98195, USA

(Received 22 November 2010; revised 8 April 2011; accepted 11 June 2011)

Reactive processes associated with multiphase flows play a significant role in mass transport in unsaturated porous media. For example, the effect of reactions on the solid matrix can affect the formation and stability of fingering instabilities associated with the invasion of a buoyant non-wetting fluid. In this study, we focus on the formation and stability of capillary channels of a buoyant non-wetting fluid (developed because of capillary instabilities) and their impact on the transport and distribution of a reactant in the porous medium. We use a combination of pore-scale numerical calculations based on a multiphase reactive lattice Boltzmann model (LBM) and scaling laws to quantify (i) the effect of dissolution on the preservation of capillary instabilities, (ii) the penetration depth of reaction beyond the dissolution/melting front, and (iii) the temporal and spatial distribution of dissolution/melting under different conditions (concentration of reactant in the non-wetting fluid, injection rate). Our results show that, even for tortuous non-wetting fluid channels, simple scaling laws assuming an axisymmetrical annular flow can explain (i) the exponential decay of reactant along capillary channels, (ii) the dependence of the penetration depth of reactant on a local Péclet number (using the non-wetting fluid velocity in the channel) and more qualitatively (iii) the importance of the melting/reaction efficiency on the stability of non-wetting fluid channels. Our numerical method allows us to study the feedbacks between the immiscible multiphase fluid flow and a dynamically evolving porous matrix (dissolution or melting) which is an essential component of reactive transport in porous media.

Key words: multiphase flow, porous media, solidification/melting

1. Introduction

Porous media flows with immiscible fluids are ubiquitous in subsurface Earth environments. The distribution and saturation level of the different fluids have a drastic effect on the dynamics of the system. The dynamics at the pore scale is controlled by capillary forces between the different fluid phases and the solid matrix. A pore-scale description of the mass transport for the different fluid phases is therefore

† Email address for correspondence: andrea.parmigiani@unige.ch

critical to better understanding of problems associated with gas and oil reservoirs, the decontamination of a polluted vadose zone (Lundegard & Andersen 1996), degassing processes in volcanic environments (Bachmann & Bergantz 2006; Huber, Bachmann & Manga 2010) and nuclear waste (Woods & Norris 2010), and CO_2 storage in a geological disposal facility (Farcas & Woods 2009; Woods & Norris 2010).

Multiphase flows in porous media are often associated with the transport of additional dissolved components (chemicals, contaminants) or heat. In many instances, their presence drives reactions at either the fluid–fluid interface (change in surface tension due to surfactants) or fluid–solid interface (dissolution/melting/precipitation due to chemical reactions and melting/solidification due to heat transfer between different phases). These reactions can ultimately affect the pore-scale geometry and lead to a local change in permeability and phase saturation. Reactions can exert a strong control on the discharge of fluids and advected quantities. The determination of the length and time scales over which reaction processes affect the porous medium have fundamental implications for matrix acidification processes in oil reservoirs, as well as the thermal evolution of a volcanic system in magmatic environments.

Mass transport in multiphase porous media flows is controlled by pressure gradients, buoyancy, viscous and capillary forces. Their relative importance determines the behaviour of the flow in the porous media. Saffman & Taylor (1958) showed that, when the invading fluid has a lower viscosity than the defending fluid, viscous fingering instability grows, leading to the development of invading fluid channels, hereafter referred to as capillary channels or fingers. On the other hand, when the viscosity of the invading fluid is comparable to or greater than that of the defending fluid, heterogeneous pore geometries and/or fluid saturation can promote the formation of capillary instabilities (e.g. Lenormand, Touboul & Zarcone 1988). The formation of channels strongly influences the macroscopic (Darcy-scale) fluid discharge. The existence of preferential pathways (channels) for the non-wetting fluid can have a disruptive influence, for example in the context of secondary oil recovery, or a positive impact for the concentration of base metals to form ore deposits.

The dynamics that control mass transport and channel formation in reactive porous media is highly nonlinear. The development of quantitative models at the pore scale, their upscaling and introduction into larger-scale transport models is a necessary step towards a better understanding of reactive porous media flows. This study aims to understand the evolution of capillary fingers in a dissolving porous medium, and characterize the effect of dissolution and dissolution rates on the transport of reactant and the local evolution of the porous medium. Laboratory experiments of multiphase flows in porous media have significantly improved our understanding of both miscible and immiscible fluid dynamics in porous media. For example, experiments of flow-front instability in homogeneous and heterogeneous porous media have been successful in testing scaling laws describing the spacing of fingers and their growth rates (see for example Homsy 1987; Glass, Steenhuis & Parlange 1989), and in studying the effect of reactions between two miscible fluids on the rheology of the mixture and its effect on the fingering dynamics (Nagatsu *et al.* 2007, 2009, 2011). However, in most cases (such as the processes studied here), the design of a suitable laboratory experiment becomes extremely challenging. As we show with our results, the dissolution rates exert primary control on the evolution of capillary fingers and, by extension, on the transport of reactant in the porous medium. Scaled experiments with slow dissolution rates, such as those characteristic of most natural systems, and, where the evolution of the system is monitored at the pore scale throughout the duration of the whole experiment, are still lacking. In this study, we therefore propose a first approach to the

pore-scale evolution of fingering instabilities in a dissolving porous medium using a combination of numerical calculations and scaling arguments.

Numerical simulations provide an attractive tool for the investigation of pore-scale processes. A wide range of numerical methods, such as dissipative particle dynamics (Hoogerbrugge & Koelman 1992), smoothed particle hydrodynamics (Gingold & Monaghan 1977) and lattice Boltzmann (LBM) (Chen & Doolen 1998) have been used, for example, to study pore-scale processes in a multiphase fluid flow environment. On the other hand, pore-network models offer a less computationally expensive alternative (these models do not resolve for interface separation between immiscible fluids), but unphysical assumptions such as fluid saturations limited to either 0 or 1 in pores rule them out for the study of reactive flows at the pore scale (Meakin & Tartakovsky 2009). In this study, we use the lattice Boltzmann method because of its ability to model single and multiphase flows in complex geometries (Martys & Chen 1996; Olson & Rothman 1997; Sukop *et al.* 2008; Boek & Venturoli 2010) and its efficiency in terms of parallelization of the algorithms (Chen & Doolen 1998).

We focus on the effect of melting on the flow of an invading buoyant non-wetting fluid in a porous medium. We use largely parallel numerical calculations and simple scaling arguments to study the formation and viability of capillary channels (channels of non-wetting fluid formed by capillary instabilities) as they transport reactant/heat through an evolving porous medium (dissolution/melting). We investigate the effect of melting on the stability of these channels and characterize the distribution of melting/reaction in the porous medium for different injection rates and melting efficiencies.

In the following section, we describe the physical model for the system under investigation and briefly introduce the conservation equations relevant to our calculations. In § 3, we present the lattice Boltzmann (LB) algorithm for thermal reactive multiphase flow in porous media developed for this study. The algorithm solves for the conservation of momentum for each fluid and the conservation of enthalpy for the three different phases (solid and the two immiscible fluids). In the fourth section, we present scaling laws and numerical results to address the question of the stability of capillary channels and the mass/heat transport associated with them.

2. Physical model

Our study focuses on the effect of reactant transported by a buoyant non-wetting fluid injected at the base of a porous medium. Because of the nonlinear nature of the problem, where the dynamical coupling between the three different phases (two immiscible fluids and solid) at the pore scale governs the evolution of the porous medium, we focus on a pore-scale, as opposed to Darcy-scale, description of the system. To simplify the following discussion, we use melting and heat transfer as an example, but the discussion applies also to dissolution problems associated with chemicals transported by the non-wetting fluid (governed by the same set of equations). We assume that a porous medium made of two different solids, one melting at a lower temperature (fertile solid fraction) and one melting at a temperature outside the range of interest in our calculations (refractory solid fraction) is initially saturated with a neutrally buoyant fluid (see figure 1). The fluid and solid are initially in thermal equilibrium at the melting temperature of the fertile solid fraction T_m. The base of the porous medium is then subjected to the injection (at a volume rate q_{nw}) of a buoyant non-wetting fluid at a temperature $T_0 > T_m$. We also raise the temperature of

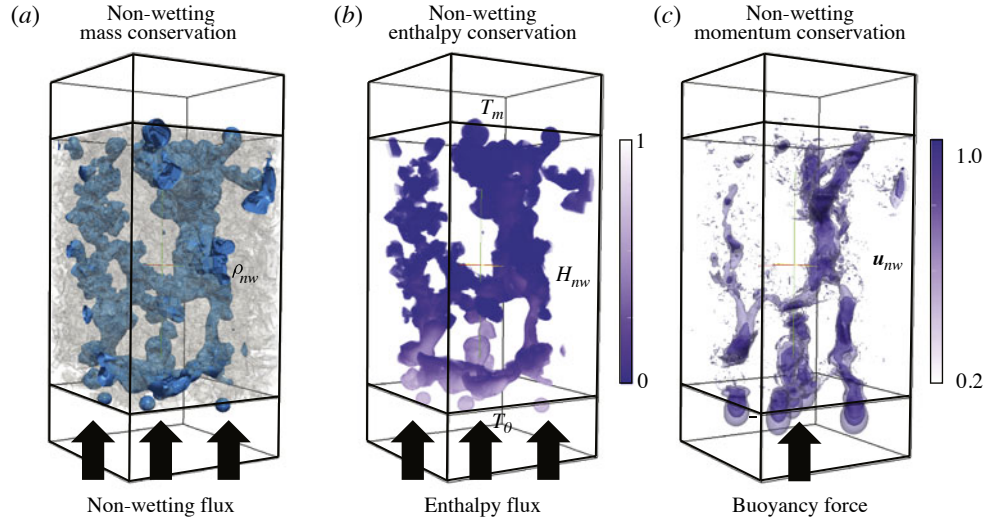

FIGURE 1. (Colour online available at journals.cambridge.org/flm) Snapshots of calculations with a Stefan number $St = 0.1$ and a local Péclet number $Pe = 42$. The porous medium contains approximately 20 000 crystals and has an initial porosity of 0.41. (*a*) Density contours for the non-wetting fluid; note the connected pathways (capillary channels). A fixed mass of buoyant non-wetting fluid is injected periodically in the inlet region (below the porous medium). (*b*) Normalized excess enthalpy (superheat) carried by the non-wetting fluid. Bubbles are injected in the inlet with a normalized superheat of 1 (0 represents the enthalpy of melting of the porous medium) and provide the heat to partially melt the porous medium. (*c*) The non-wetting fluid velocity (here the magnitude) is controlled by the geometry of the pathways, the buoyancy (Bond number) and the injection rate (capillary pressure).

the boundary condition at the base of the porous medium to T_0 (thermal equilibrium with the bubbles of injected non-wetting fluid).

The heat transferred from the lower boundary and from the ascending non-wetting fluid bubbles is transferred to the wetting fluid and porous matrix resulting in the partial dissolution/melting of the latter. Because of capillary forces and heterogeneities in the pore-size distribution of the porous medium, capillary instabilities develop and control the spatial distribution of the invading non-wetting fluid and therefore the localization of melting. The viscosity ratio between the two fluids can have a strong influence on the development of capillary instability and the discharge of non-wetting fluid through the porous medium. Our calculations assume for simplicity a viscosity ratio of 1 between the two fluid phases; the importance of the viscosity ratio will be assessed in further studies.

The problem we are solving is described by mass conservation for each of the two fluids and the solid fraction in the porous medium,

$$\frac{\partial \rho_s(\boldsymbol{x})}{\partial t} = -\Gamma_m(\boldsymbol{x}), \tag{2.1}$$

$$\frac{\partial \rho_w(\boldsymbol{x})}{\partial t} + \boldsymbol{\nabla} \cdot (\rho_w(\boldsymbol{x})\boldsymbol{u}_w(\boldsymbol{x})) = \Gamma_m(\boldsymbol{x}), \tag{2.2}$$

$$\frac{\partial \rho_{nw}(\boldsymbol{x})}{\partial t} + \boldsymbol{\nabla} \cdot (\rho_{nw}(\boldsymbol{x})\boldsymbol{u}_{nw}(\boldsymbol{x})) = \Gamma_{inj}(\boldsymbol{x}), \tag{2.3}$$

where Γ_m is the melting rate, Γ_{inj} is the mass injection rate of non-wetting fluid, ρ_s, ρ_w and ρ_{nw} are respectively the local density of solid, wetting and non-wetting fluids, $\boldsymbol{u}_w$ and $\boldsymbol{u}_{nw}$ are the wetting and non-wetting fluid velocities. The injection rate of non-wetting fluid can be described in terms of an injection capillary number $Ca = q_{nw}\mu_{nw}/(\gamma R^2)$ (Lenormand *et al.* 1988; Ewing & Berkowitz 1998), where q_{nw} is the volume rate of injected non-wetting fluid, γ is the surface tension between the two fluids and R is a reference length scale here fixed to the average pore radius size. Defining the local injection rate per unit volume ϕ_q,

$$q_{nw} = \int_V \phi_q \, \mathrm{d}V, \tag{2.4}$$

where the volume V here includes the porous medium plus the inlet and outlet chambers, Γ_{inj} becomes

$$\Gamma_{inj} = \rho_{nw}\phi_q, \qquad \int_V \Gamma_{inj} \, \mathrm{d}V = \frac{\rho_{nw}\gamma R^2 Ca}{\mu_{nw}}. \tag{2.5}$$

Momentum conservation for the two fluids yields

$$\frac{\partial \rho_w(\boldsymbol{x})\boldsymbol{u}_w(\boldsymbol{x})}{\partial t} + (\rho_w(\boldsymbol{x})\boldsymbol{u}_w(\boldsymbol{x}) \cdot \nabla)\boldsymbol{u}_w(\boldsymbol{x}) = \nabla \cdot \boldsymbol{T}_w(\boldsymbol{x}) + \Phi_w(\boldsymbol{x}), \tag{2.6}$$

$$\frac{\partial \rho_{nw}(\boldsymbol{x})\boldsymbol{u}_{nw}(\boldsymbol{x})}{\partial t} + (\rho_{nw}(\boldsymbol{x})\boldsymbol{u}_{nw}(\boldsymbol{x}) \cdot \nabla)\boldsymbol{u}_{nw}(\boldsymbol{x}) = \nabla \cdot \boldsymbol{T}_{nw}(\boldsymbol{x}) + \Phi_{nw}(\boldsymbol{x}), \tag{2.7}$$

where $\boldsymbol{T}$ is the stress tensor, Φ_w and Φ_{nw} are inertial terms associated with, respectively, melting and injection:

$$\Phi_w(\boldsymbol{x}) = \Gamma_m(\boldsymbol{x})\boldsymbol{u}_w(\boldsymbol{x}), \tag{2.8}$$

$$\Phi_{nw}(\boldsymbol{x}) = \Gamma_{inj}(\boldsymbol{x})\boldsymbol{u}_{nw}(\boldsymbol{x}). \tag{2.9}$$

The stress tensor for each fluid phase is given by

$$\boldsymbol{T}_i = -p\boldsymbol{I} + \mu_i(\nabla \boldsymbol{u}_i + \nabla \boldsymbol{u}_i^T) + \rho_i(\boldsymbol{g} \cdot \boldsymbol{x})\boldsymbol{I}, \tag{2.10}$$

where $\boldsymbol{I}$ is the identity matrix, p is the pressure and $\boldsymbol{g}$ is the acceleration due to gravity. Normalizing velocities by $\mathscr{U} = (\rho_w - \rho_{nw})gR^2/\mu_w$ and length scales by the average pore radius R, the stress jump associated with surface tension at the interface between the two fluids becomes (Stone & Leal 1990; Pozrikidis 1992; Manga & Stone 1993)

$$\boldsymbol{n} \cdot \boldsymbol{T}_w^*(\boldsymbol{x}) - \lambda \boldsymbol{n} \cdot \boldsymbol{T}_{nw}^*(\boldsymbol{x}) = \frac{1}{Bo}(\nabla_s \cdot \boldsymbol{n})\boldsymbol{n} - (\hat{\boldsymbol{g}} \cdot \boldsymbol{x})\boldsymbol{n}, \tag{2.11}$$

where the superscript $*$ refers to a dimensionless variable, $\boldsymbol{x}$ is located at the interface between the two fluids, $\boldsymbol{n}$ is the outward normal to the interface, ∇_s is the gradient along the interface, $Bo = \Delta\rho g R^2/\gamma$ is the Bond number and $\lambda = \mu_{nw}/\mu_w$.

Finally, we solve for the conservation of enthalpy for the three phases

$$\frac{\partial(\rho_s c_s T_s)}{\partial t} = -\nabla \cdot \boldsymbol{Q}_s, \tag{2.12}$$

$$\frac{\partial(\rho_w c_w T_w)}{\partial t} = -\nabla \cdot \boldsymbol{Q}_w, \tag{2.13}$$

$$\frac{\partial(\rho_{nw} c_{nw} T_{nw})}{\partial t} = -\nabla \cdot \boldsymbol{Q}_{nw}, \tag{2.14}$$

where T_i refers to the temperature of phase i, c_i to the specific heat and $\boldsymbol{Q}_i$ the heat flux

$$\boldsymbol{Q}_s(\boldsymbol{x}) = -k_s \nabla T_s(\boldsymbol{x}), \tag{2.15}$$

$$\boldsymbol{Q}_w(\boldsymbol{x}) = \rho_w(\boldsymbol{x}) c_w \boldsymbol{u}_w(\boldsymbol{x}) T_w(\boldsymbol{x}) - k_w \nabla T_w(\boldsymbol{x}), \tag{2.16}$$

$$\boldsymbol{Q}_{nw}(\boldsymbol{x}) = \rho_{nw}(\boldsymbol{x}) c_{nw} \boldsymbol{u}_{nw}(\boldsymbol{x}) T_{nw}(\boldsymbol{x}) - k_{nw} \nabla T_{nw}(\boldsymbol{x}), \tag{2.17}$$

with k_i the thermal conductivity of phase i. Melting is introduced by matching the heat fluxes across the solid–fluid interfaces. Using the same velocity and length scales as for the stress jump at the fluids interface, we obtain an explicit formulation for $\Gamma_m(\boldsymbol{x})$:

$$\begin{aligned} &\boldsymbol{u}_w^*(\boldsymbol{x}) T_w^*(\boldsymbol{x}) - \frac{1}{\xi \lambda Pe} \nabla^* T_w^*(\boldsymbol{x}) + \Lambda \boldsymbol{u}_{nw}^*(\boldsymbol{x}) T_{nw}^*(\boldsymbol{x}) - \frac{1}{Pe} \nabla^* T_{nw}^*(\boldsymbol{x}) \\ &\quad = -\frac{1}{\mathscr{A}} \nabla^* T_s^* + \frac{1}{\lambda St} \mathscr{B} \Gamma_m(\boldsymbol{x}), \end{aligned} \tag{2.18}$$

where $St = c_{nw}(T_0 - T_m)/L_f$, T_0 is the temperature of the non-wetting fluid at the injection, T_m is the melting temperature of the fertile fraction of the porous medium ($T_0 > T_m$), L_f is the latent heat of fusion, $\Lambda = \rho_{nw} c_{nw}/(\rho_w c_w)$, $\xi = \kappa_{nw}/\kappa_w$, $Pe = \mathscr{U} R/(\kappa_{nw})$ is the Péclet number for the non-wetting fluid, $\mathscr{A} = \rho_w c_w R \mathscr{U}/k_s$ and $\mathscr{B} = (\rho_w \mathscr{U} R^2)^{-1}$. In (2.18), we assumed that the fertile solid fraction melts as a pure substance (fixed melting temperature T_m), similarly to a Stefan problem.

This set of governing equations, together with the set of stress and heat transfer boundary conditions between the different phases, fully describes the dynamical evolution of the system for a given (evolving) porous matrix geometry. The following section presents the numerical strategy we developed to solve this complex and highly coupled set of equations.

3. Numerical model

Our choice of numerical method is dictated by the necessity of solving for the multiphase dynamics at the pore scale (i) to avoid resorting to poorly constrained constitutive equations, and (ii) to solve for the reactive process and the feedback between flow and reactant transport associated with melting/dissolution. The field of multiphase flows in porous media has an extensive literature, an important part of which is devoted to numerical models for investigating fingering phenomena in porous media. A first class of model assumes a Darcy-scale description of the multiphase flow and is based on various extensions of the Richards equation (RE). The stability of the standard RE to fingering has been shown and demonstrated rigorously by Eliassi & Glass (2001), Egorov *et al.* (2003), van Duijn, Pieters & Raats (2004), Nieber *et al.* (2005) and Fürst *et al.* (2009). Several authors have modified RE successfully to reproduce fingering instabilities observed in the context of laboratory experiments (Nieber *et al.* 2003, 2005). Chapwanya & Stockie (2010) showed that, in the context of RE, the growth of fingering instabilities requires the inclusion of non-equilibrium effects to correct for the evolution of the capillary pressure in response to saturation changes. This is usually done by introducing a relaxation to equilibrium, but the choice of the relaxation functional form remains an open question (Chapwanya & Stockie 2010). Cueto-Felgueroso & Juanes (2008, 2009*a*,*b*) used a different approach in analogy with low-Reynolds-number gravity currents (Huppert 1982) to justify the introduction of an additional term in RE that allows for fingering instabilities to grow. Nevertheless, the latter model still requires constitutive equations to account for pore-scale effects at the Darcy scale, such as the relative permeability–saturation

relationship and the macroscopic surface tension. These constitutive equations are very sensitive to the topology of the porous medium and, for realistic geometries, cannot be derived from first principles.

Another field of numerical investigations for the invasion of a fluid in a saturated porous medium is based on pore-network models (Lenormand *et al.* 1988; Ewing & Berkowitz 1998; Blunt 2001). These models solve a simplified dynamics at the pore scale, where every pore is fully saturated by one phase or the other. The capillary coupling between the two phases is then greatly simplified. The scale of resolution of these models is one node per pore, no gradients of flow velocity or scalar fields can be computed, and as a result these models cannot solve for solute transport by one of the two fluid phases.

The ideal choice of numerical method for the present study is dictated by the following considerations: (i) the ability to compute the multiphase dynamics at the pore scale, (ii) the ability to handle complex-moving boundaries in a simple and consistent fashion, fluid–fluid and fluid–solid interfaces, (iii) the ability to deal with bubble coalescence and breakup, and (iv) efficient parallelization so that the number of pores is large enough to draw significant results from the calculations. Several numerical methods have been proposed to solve the pore-scale dynamics explicitly, such as the volume of fluid (Hirt & Nichols 1981; Huang, Meakin & Liu 2005) and level set methods (Osher & Sethian 1988). These methods usually require a front-tracking algorithm for the fluid–fluid interface and become computationally intense when dealing with a large number of bubbles, with coalescence and breakup and bounded by a complex (and for us time-dependent) solid topology. Meakin & Tartakovsky (2009) present a discussion of the advantages and limitations of various numerical techniques for pore-scale reactive flow calculations, they highlight that the lattice Boltzmann method offers an efficient alternative for large-scale computations of multiphase flows in complex porous media. Another advantage of using LB models for immiscible flows over models based on Darcy-scale approximations or pore-network models, is that it allows us to resolve pore-scale dynamics and moving boundaries (melting) naturally (Huber *et al.* 2008).

3.1. *The lattice Boltzmann equation and the Bhatnagar–Gross–Krook collision operator*

The quantity of interest in the lattice Boltzmann method is the discrete particle distribution function f_i. In analogy with statistical mechanics, $f_i(\boldsymbol{x}, t)$ expresses the probability of finding a particle that enters a lattice node $\boldsymbol{x}$ at time t along a given lattice velocity $\boldsymbol{v}_i$ (set of vectors connecting nearest neighbours lattice nodes, along which the f_i are allowed to stream). The evolution of the f_i is described by a discrete version of the Boltzmann equation. In general, the complex collision term in Boltzmann's equation is replaced by the simple BGK approximation (Bhatnagar, Gross & Krook 1954), the discrete Boltzmann equation becomes

$$f_i(\boldsymbol{x} + \boldsymbol{v}_i \Delta t, t + \Delta t) - f_i(\boldsymbol{x}, t) = -\omega(f_i(\boldsymbol{x}, t) - f_i^{eq}(\boldsymbol{x}, t)) \tag{3.1}$$

where Δt is the discrete time step. The first term on the right-hand side of (3.1) represents the BGK rule for collision between the f_i. The BGK collision expresses how the f_i, after collision, relax to the local equilibrium distribution function f_i^{eq} with a single relaxation frequency ω. The choice of relaxation frequency ω controls the kinematic viscosity of the fluid

$$\frac{\mu}{\rho} = c_s^2 \frac{\Delta x^2}{\Delta t} \left(\frac{1}{\omega} - \frac{1}{2} \right), \tag{3.2}$$

where c_s^2 is the sound speed of the lattice (a constant that depends on the spatial discretization used) and Δx is the grid spacing. The f_i^{eq} are obtained from a second-order Taylor expansion of the Maxwell–Boltzmann distribution. An additional source/sink term Ξ_i can be introduced into the right-hand side of (3.1). This source/sink term allows us to include reactive processes (Kang, Lichtner & Zhang 2006; Huber *et al.* 2008) or external body forces (Guo, Zheng & Shi 2002*b*; Latt *et al.* 2010). In order to model complex natural systems, the governing equations have to be properly coupled. We use a multi-distribution function (MDF) approach (Shan 1997; Guo, Shi & Zheng 2002*a*; Parmigiani *et al.* 2009) to address this particular issue. In the MDF approach, any conservation law associated with different transport properties (i.e. viscosity, diffusivity etc.) is described with a different set of particle distribution functions f_i.

In this study, we developed a lattice Boltzmann model that couples a well-established multiphase flow model (multi-component Shan–Chen method: Shan & Chen 1993) with a thermal model that solves for the enthalpy conservation in a porous medium. The thermal model we use allows for melting (dissolution) of the solid matrix and is based on the melting model of Huber *et al.* (2008). Although the individual components (melting, multiphase flow) of the numerical model have been tested and validated in other studies (see the validation section below), their combination is new and allows us to investigate the pore-scale evolution of a porous medium subjected to dissolution during the invasion of a reactive non-wetting fluid. Understanding the possible feedbacks between capillary instabilities (Saffman–Taylor instability) that enhance the transport of reactant and dissolution which affects the evolution of the capillary fingers is challenging and, to our knowledge, this is the first attempt to quantify these processes.

In order to obtain results that are significant beyond the pore scale (to introduce corrections into Darcy equation), we use a crystal nucleation and growth algorithm derived from the model of Avrami (1940) and modified by Hersum & Marsh (2006) to generate a crystalline porous matrix that is large enough (order of several thousands of pores) to yield statistically significant results. In this work, all calculations used a synthetic porous media matrix composed with ∼20 000 crystals with various shapes and sizes representing a grid with $200 \times 200 \times 300$ lattice nodes (see figure 2). The mean pore radius is ∼10 grid nodes (this length scale will be used later as the characteristic length to normalize distances). In this work, we build a solid matrix with two different crystal species, assuming that they have different melting temperatures. The first type of crystal occupies initially 38 % (see figure 2*a*) of the sample volume and has a melting temperature $T = T_m$ that corresponds to the initial temperature of the wetting fluid and porous medium. The second crystal family represents 21 % (see figure 2*b*) of the sample volume, and was set with a melting temperature such that it will never melt during the course of our calculations.

The initial porosity of our synthetic sample is 0.41 (see figure 2). This lattice size and the number of distribution functions involved are computationally challenging. The local nature of the LB and the efficiency of the code we used, based on the Palabos platform (Palabos 2010), allowed us to perform approximately 60 calculations at four different *St* numbers and four different *Pe* numbers, where each simulation was run on 2000 processors for running times ranging from 12 to 60 h.

3.2. *LB scheme for immiscible fluid flows in porous media*

The lattice Boltzmann community has developed a variety of models for multiphase and multi-component fluid flow applications. These different LB algorithms can be

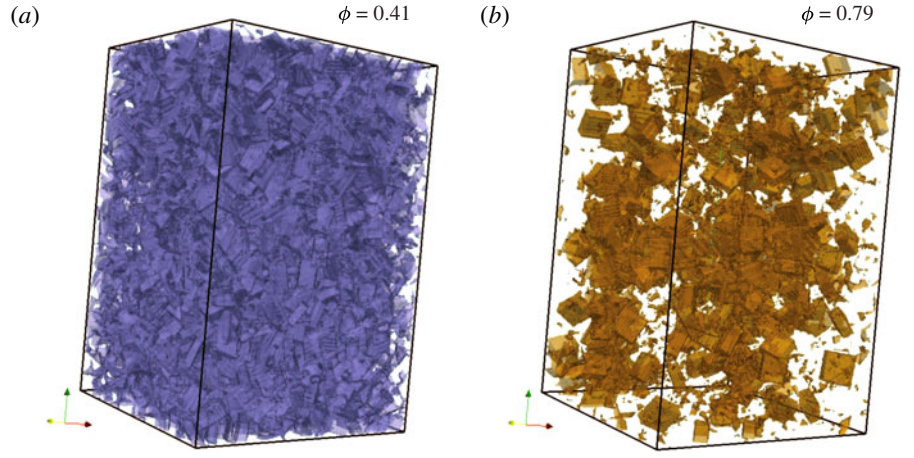

FIGURE 2. (Colour online) Solid fraction of the porous medium for this study. The initial porosity ϕ is 0.41. The texture is composed of two different solids. The first family of 'crystals', hereafter called the fertile fraction, is set initially at its melting temperature (pure substance melting) and represents $\sim$38 % of the sample volume. The second family, hereafter called the refractory fraction, occupies 21 % of the sample volume and never melts during our calculations.

grouped into two classes depending on their approach to modelling non-ideal fluid behaviours. In a first class of models (Swift *et al.* 1996; He, Chen & Zhang 1999), the definition of a free energy function is required. This choice leads to a continuum mathematical formulation described by the Cahn–Hilliard theory (Cahn & Hilliard 1958). A second class of models is based on first principles for the microscopic interaction between the two fluids (Gunstensen *et al.* 1991; Shan & Doolen 1995). These models converge to the continuum mass and momentum conservation for a slightly compressible multi-component mixture of fluids (Shan & Doolen 1995).

All these models, however, belong to a more general class diffuse-interface methods (Anderson, McFadden & Wheeler 1998). For the case of an immiscible binary mixture, this means that when the equilibrium state is reached, the two fluids are separated by an interface of finite thickness δ. The mean field nature of the LB algorithms allows us to study capillary effects between the different phases (e.g. deformable interfaces, coalescence processes) without having to track the evolution of a deformable interface in complex geometries, in contrast to volume of fluid (Hirt & Nichols 1981; Huang *et al.* 2005) or level set methods (Osher & Sethian 1988).

For this work, we use the multi-component Shan–Chen (S–C) method for immiscible fluid flow (Shan & Chen 1993; Shan & Doolen 1995). This model has been applied successfully to the study of capillary instabilities (Hagedorn, Martys & Douglas 2004) and wetting properties in both static and dynamic settings for both two-dimensional and three-dimensional geometries (Kang, Zhang & Chen 2005; Huang *et al.* 2007). Furthermore, the implementation of no-slip surfaces on the solid matrix is straightforward, it is accomplished by a reflection of the incoming particle distribution function on solid nodes (bounce-back method), and favours this model for multi-component fluid flow application in porous media. For example, the S–C scheme has been applied to invasion percolation processes and the determination of relative permeabilities for packed sphere as well as more complex natural geometries (Martys & Chen 1996; Olson & Rothman 1997; Sukop & Or 2003; Pan, Hilpert & Miller 2007; Schaap *et al.* 2007; Sukop *et al.* 2008; Boek & Venturoli 2010). A few studies,

however, underline a lack of flexibility and accuracy of the method when fluids with different viscosities are investigated (Chin, Boek & Coveney 2002; Grosfils, Boon, Chin & Boek 2004).

For the case of the S–C binary mixture model, $f_i^{nw,eq}$ and $f_i^{w,eq}$ are defined by

$$f_i^{\sigma,eq}(\boldsymbol{x},t) = w_i\rho_\sigma\left[1+\frac{\boldsymbol{v}_i\cdot\boldsymbol{u}_\sigma^{eq}}{c_s^2}+\frac{(\boldsymbol{v}_i\cdot\boldsymbol{u}_\sigma^{eq})^2}{2c_s^4}-\frac{\boldsymbol{u}_\sigma^{eq^2}}{2c_s^2}\right], \tag{3.3}$$

where c_s is a constant characteristic of the lattice topology called speed of sound and $\sigma = nw, w$. The density and momentum for each component σ are defined by $\rho_\sigma = \sum_i f_i^\sigma$ and $\rho_\sigma \boldsymbol{u}_\sigma = \sum_i \boldsymbol{v} f_i^\sigma \cdot \boldsymbol{u}_\sigma^{eq}$ in (3.3) is determined by the relation

$$\boldsymbol{u}_\sigma^{eq} = \frac{\sum_\sigma \rho_\sigma \boldsymbol{u}_\sigma \omega_\sigma}{\sum_\sigma \rho_\sigma \omega_\sigma} + \frac{\boldsymbol{F}_\sigma}{\omega_\sigma \rho_\sigma}, \tag{3.4}$$

where $\boldsymbol{F}_\sigma = \boldsymbol{F}_\sigma^{coh} + \boldsymbol{F}_\sigma^{ads} + \boldsymbol{F}_\sigma^{b}$ is a sum over the fluid–fluid and fluid–solid interaction forces, $\boldsymbol{F}_\sigma^{coh}$ are the cohesion forces responsible for phase separation and surface tension, $\boldsymbol{F}_\sigma^{ads}$ are the adhesion forces between the solid boundaries and the fluids, and $\boldsymbol{F}_\sigma^{b}$ are the external body forces.

In the S–C method the interaction force between the different phases (the cohesion forces) is given by

$$\boldsymbol{F}_\sigma^{coh}(\boldsymbol{x},t) = -\rho_\sigma(\boldsymbol{x},t)G^{coh}\sum_i w_i\rho_{\bar\sigma}(\boldsymbol{x}+\boldsymbol{v}_i\Delta t)\boldsymbol{v}_i, \tag{3.5}$$

where σ and $\bar\sigma$ are, respectively, the first and second fluid phases, G^{coh} is a free parameter that controls the surface tension between the two fluids and ρ is the density of the fluid.

Similarly, the adhesion force between particles of the fluid σ and the solid boundary, can be calculated with

$$\boldsymbol{F}_\sigma^{ads}(\boldsymbol{x},t) = -\rho_\sigma(\boldsymbol{x},t)G_\sigma^{ads}\sum_i w_i s_{\bar\sigma}(\boldsymbol{x}+\boldsymbol{v}_i\Delta t)\boldsymbol{v}_i, \tag{3.6}$$

where the solid nodes are represented as a phase with constant density s. G_σ^{ads} determines the strength of the interaction between particles of species σ and the solid boundary, and, as a consequence, governs the wetting properties of the fluid.

Body forces can be introduced with

$$\boldsymbol{F}_\sigma^{b}(\boldsymbol{x},t) = \Delta\rho_\sigma \boldsymbol{g}, \tag{3.7}$$

where $\boldsymbol{g}$ is the body force per unit mass. The body force term can be used to implement buoyancy force effects due to density difference between different phases (which in our calculations greatly exceed thermal expansion effects). The local density and velocity of the multiphase mixture can be respectively calculated with

$$\rho^{tot} = \sum_\sigma \rho_\sigma, \quad \boldsymbol{u}^{tot} = \frac{1}{\rho^{tot}}\left[\left(\sum_\sigma\sum_i f_i^\sigma v_i\right)+\frac{1}{2}\sum_\sigma \boldsymbol{F}_\sigma\right]. \tag{3.8}$$

For three-dimensional calculations, we use a lattice topology with 19 velocities for both fluids (the so-called D3Q19 lattice). In the D3Q19 lattice, the velocities vectors

linking neighbour nodes $\boldsymbol{v}_i$ and weights w_i are given by

$$\boldsymbol{v}_i = \begin{cases} (0,0,0), & i=0, \\ (\pm1,0,0),(0,\pm1,0),(0,0,\pm1), & i=1\text{–}6, \\ (\pm1,\pm1,0),(\pm1,0,\pm1),(0,\pm1,\pm1), & i=7\text{–}18, \end{cases} \tag{3.9}$$

$$w_0 = 1/3, \quad w_{1\text{–}6} = 1/18, \quad w_{7\text{–}18} = 1/36. \tag{3.10}$$

The speed of sound c_s for this lattice is equal to $\sqrt{1/3}$.

3.3. *Pure substance melting*

Our study focuses on modelling the exchange of heat between the solid, wetting and non-wetting phases. For simplicity, we assume that the wetting fluid and the fertile solid are two phases of the same pure substance. The enthalpy conservation is modelled with a single relaxation time LB passive scalar approach (Chopard, Falcone & Latt 2009). The algorithm for the evolution of the enthalpy (temperature and melt fraction) is similar to (3.1). We define a new set of particle distribution functions g_i evolving according to (3.1). The proper choice of equilibrium distribution for an advection–diffusion process is

$$g_i^{eq} = s_i T \left(1 + \frac{1}{c_s^2} \boldsymbol{e}_i \cdot \boldsymbol{u}^{tot}\right), \tag{3.11}$$

where $\boldsymbol{e}_i$ and s_i are the lattice velocities and weights specific for this model. The enthalpy is defined by $\mathscr{H} = cT + f_l L_f$, where c is the specific heat, T is the temperature, f_L is the local liquid fraction ($0 \leqslant f_L \leqslant 1$) and L_f is the latent heat of fusion of the solid phase. Heat is advected with the local fluid velocity $\boldsymbol{u}^{tot}$ (see (3.8)), and diffuses with diffusion coefficient $\kappa = c_s^2 \Delta x^2 \left(1/\omega_h - 0.5\right)/\Delta t$, where ω_h is the relaxation frequency similarly to (3.1) .

We assume that the thermal diffusivity for the solid and wetting fluid is identical and we impose a constant diffusivity ratio $\xi = \kappa_w/\kappa_{nw} = 7$, where κ_w and κ_{nw} are the thermal diffusivities for the wetting and non-wetting phases, respectively. The choice for this thermal diffusivity ratio is arbitrary, but in the present study, it is motivated by the application where hot volatiles exsolved from a new injection of magma rise through a colder and more crystal-rich magma chamber, which has been hypothesized to play an important role in the thermal evolution of magmatic systems in the shallow crust (Bachmann & Bergantz 2006; Huber *et al.* 2010)

Based on the enthalpy method (Patankar 1980), we model the pure substance phase change between the fertile solid fraction and the wetting fluid by introducing a source (crystallization) or sink (melting) term Ξ_i as in Huber *et al.* (2008). The temperature and the local enthalpy are obtained respectively as

$$T(\boldsymbol{x},t) = \sum_i = g_i(\boldsymbol{x},t), \quad \mathscr{H}(\boldsymbol{x},t) = cT(\boldsymbol{x},t) + L_f f_l(\boldsymbol{x},t-1). \tag{3.12}$$

In the melting algorithm, once $\mathscr{H}(\boldsymbol{x},t)$ is obtained, it is used to calculate the new melt fraction f_l at time step t:

$$f_l = \begin{cases} 0 & \mathscr{H} < \mathscr{H}_s = cT_m, \\ \dfrac{\mathscr{H} - \mathscr{H}_s}{\mathscr{H}_l - \mathscr{H}_s} & \mathscr{H}_s \leqslant \mathscr{H} \leqslant \mathscr{H}_s + L_f, \\ 1 & \mathscr{H} > \mathscr{H}_s + L_f. \end{cases} \tag{3.13}$$

In (3.13) $\mathscr{H}_l$ and $\mathscr{H}_s$ correspond to the enthalpy of the liquidus and solidus respectively. Using this framework, Ξ_i is calculated with

$$\Xi_i = s_i \frac{L_f}{c}(f_l(\boldsymbol{x}, t) - f_l(\boldsymbol{x}, t-1)). \tag{3.14}$$

In our three-dimensional calculations, we use a seven-velocity lattice (D3Q7), for which $c_s = 1/4$, and the discrete velocities $\boldsymbol{e}_i$ and weights are

$$\boldsymbol{e}_i = \begin{cases} (0,0,0) & a = 0, \\ (\pm 1,0,0),\ (0,\pm 1,0),\ (0,0,\pm 1) & a = 1-6, \end{cases} \tag{3.15}$$

$$s_0 = 1/4, \quad s_1 = s_2 = s_3 = s_4 = s_5 = s_6 = 1/8. \tag{3.16}$$

3.4. *Validation*

Our numerical model has been constructed incrementally and combines well-established algorithms, e.g. the Shan–Chen model for multiphase flows, with numerical models we developed and published recently, e.g. the advection–diffusion model with pure substance melting (Shan & Chen 1993; Huber *et al.* 2008). The nonlinearity of the pore-scale dynamics of multiphase flows in a slowly dissolving porous medium prevented us from directly comparing the model to either analytical solutions or laboratory experiments. The lack of published results for laboratory experiments investigating the effect of matrix dissolution on the evolution of capillary fingers prevents a comparison with our numerical results: this issue can be explained by the difficulty of designing suitable experiments. First, as our results show (see next section), the dissolution rate has a strong influence on the overall evolution of the multiphase flow. Natural applications are generally characterized by slow dissolution processes, such as, for example, the thermal evolution of crystal-rich magma bodies (crystal mush) in the shallow crust during the buoyant invasion of hot volatiles exsolved by new injections of magma ($St < 0.1$). In that context, the monitoring of the flow field at the pore scale during scaled experiments (at least in terms of dissolution rates St), is challenging. Our validation methodology is therefore restricted to testing the different components (melting, multiphase fluid dynamics) of the numerical model individually on simpler problems. We present below a list of benchmark calculations our model was tested with, and, when necessary, refer to published results for well-established algorithms (the Shan–Chen multiphase model).

Huber *et al.* (2008) extended the model of Jiaung, Ho & Kuo (2001) for conduction melting to the problem of melting by both advection and diffusion. The algorithm has been benchmarked, first, with the Stefan problem for one-dimensional diffusion, where numerical solutions can be compared to the analytical solution found by Neumann. Figure 3 shows a comparison of the propagation of the melting front and snapshots of temperature profiles with the analytical solutions for different (dimensionless) thermal diffusivities. Lower dimensionless diffusivities yield a more accurate result as they are equivalent with calculations with shorter time steps. Huber *et al.* (2008) also successfully tested the numerical model for melting in a square, initially solid enclosure, where natural convection is initiated. This problem has been the subject of laboratory experiments (Bénard, Gobin & Martinez 2006), and the focus of a theoretical study by Jany & Bejan (1988). Moreover, different studies used this problem as a numerical benchmark for moving boundary calculations (see for example Bertrand *et al.* 1999; Bénard *et al.* 2006). Figure 4 shows an example of the temporal evolution of the melting enclosure (first two rows, heated well on the left) and a snapshot to reveal the temperature, melt fraction and velocity field in the partially

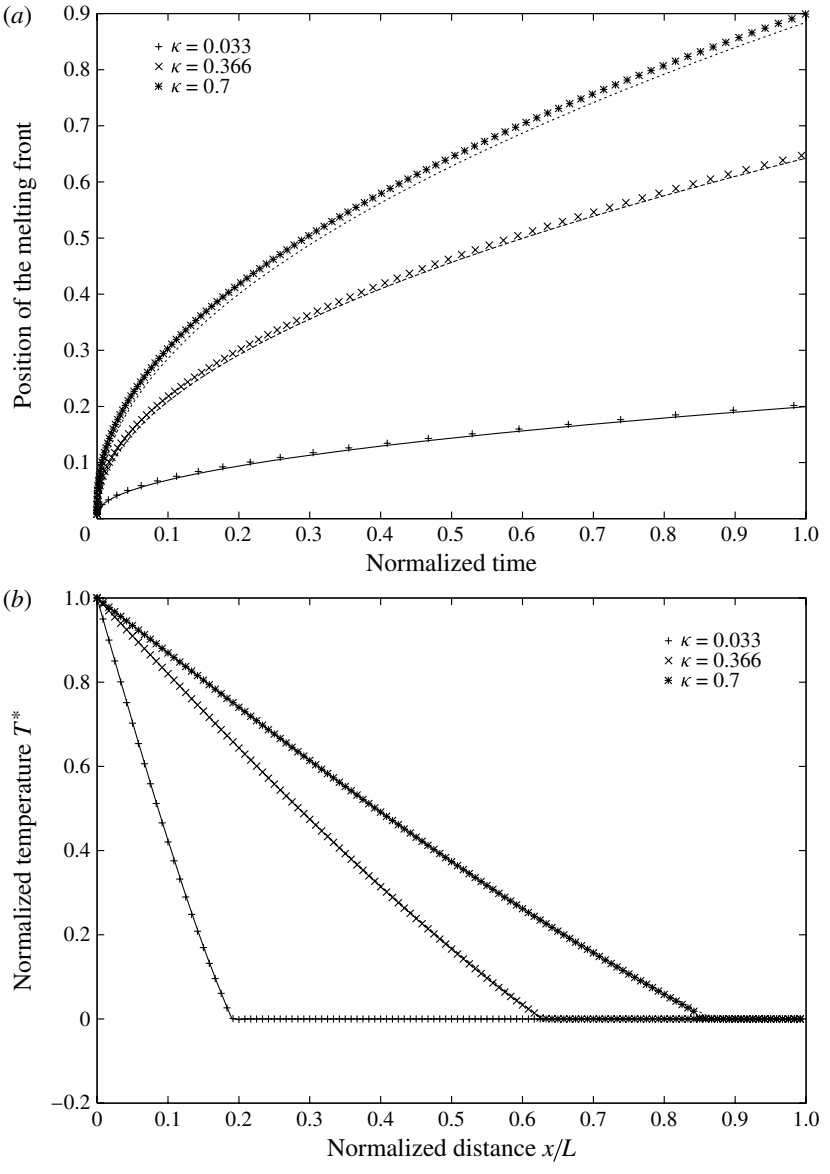

FIGURE 3. Comparison of the melting front position and temperature profiles between the melting LB model (crosses) and analytical solutions (solid curves) for three thermal diffusivities (κ, in lattice units) with Stefan number $St = 1$ (second row) and $St = 10$ (third row). Time is made dimensionless in order to compare the sensitivity of the model to the size of the time steps. From Huber *et al.* (2008).

molten enclosure. Huber *et al.* (2008) showed that their numerical model was in good agreement with the scaling relationships of Jany & Bejan (1988), with experimental results (Bénard *et al.* 2006) and with results obtained with front-tracking numerical models (Bertrand *et al.* 1999). For more details about the accuracy and stability of the model, readers are referred to Huber *et al.* (2008).

The multiphase flow model we chose, the Shan–Chen model, has been used extensively over the last decade. It has been tested successfully for both static and

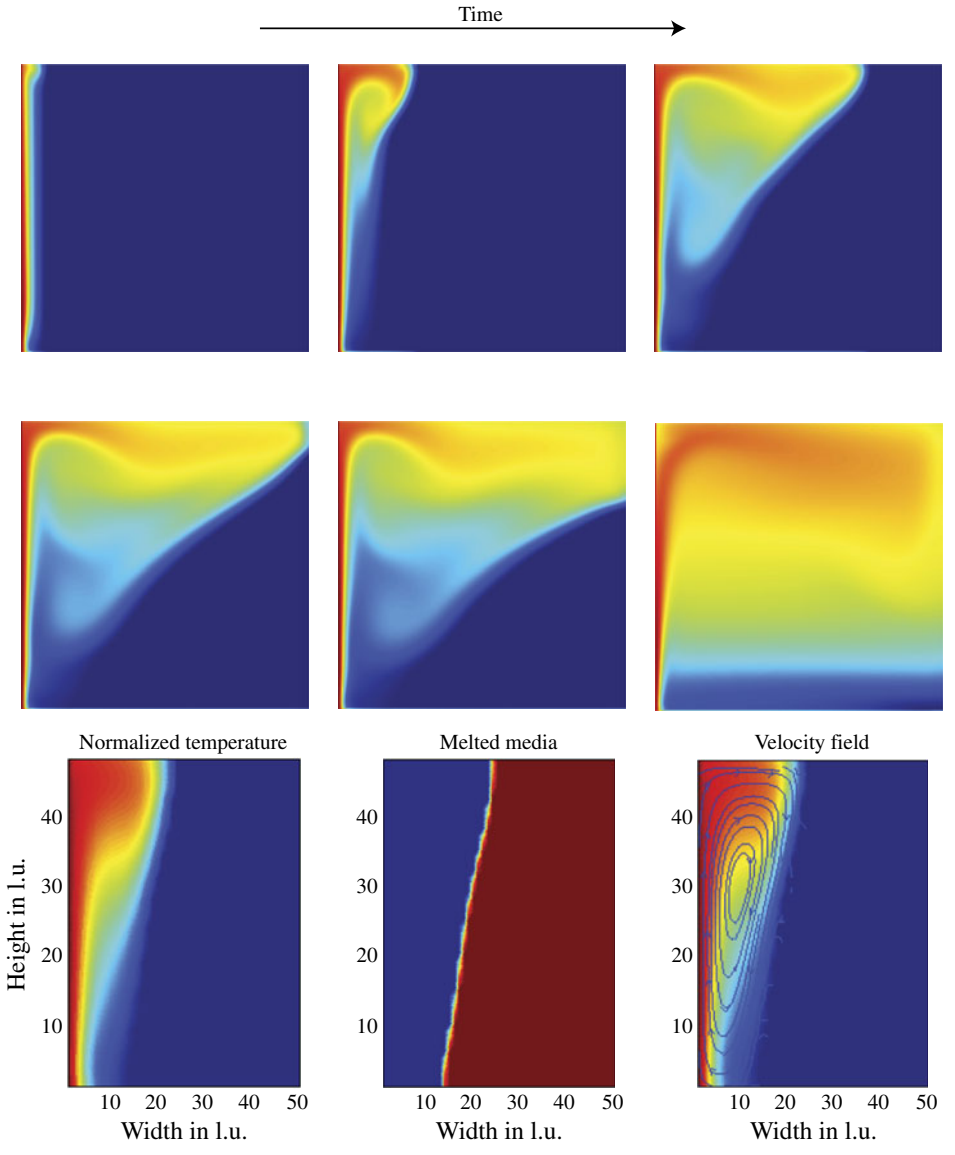

FIGURE 4. (Colour online) Example of natural convection melting in a square enclosure. The left wall is kept at constant temperature (above the melting temperature of the solid) and the whole enclosure is solid initially. Convection develops and leads to the propagation of the melting front to the right (faster at the top of the enclosure because of convection). These calculations have been benchmarked with other numerical models, laboratory experiments and scaling relationships; for more details see Huber *et al.* (2008). l.u., lattice units.

dynamical problems (Kang *et al.* 2005; Huang *et al.* 2007). In figure 5(*a*), we show a two-dimensional static validation of the model with the Laplace–Young law, which predicts a linear relationship between the pressure difference across the fluid–fluid interface and the radius of the bubble. Figure 5(*b*) shows the dependence of the surface tension on the free parameter G^{coh} in two dimensions. Similar validations for

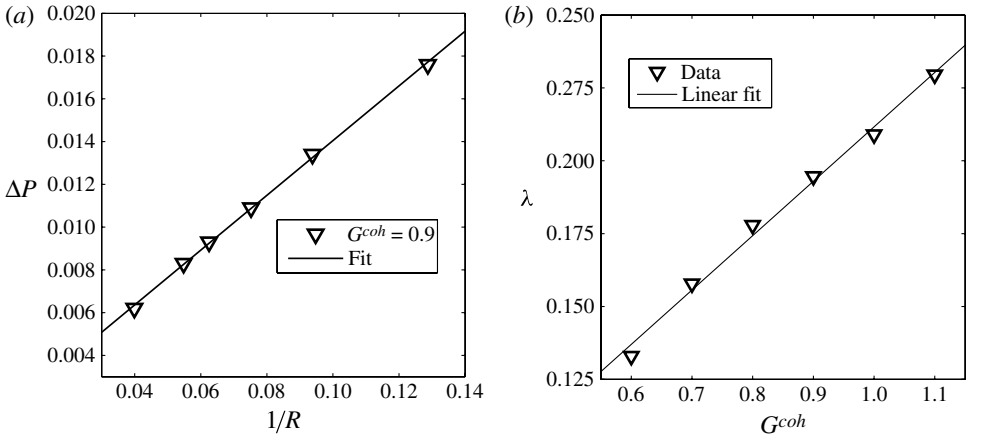

FIGURE 5. (*a*) Pressure drop ΔP across the bubble interface as a function of $1/R$ (where R is the bubble radius) for a two-dimensional case. The bubble is placed in the middle of a 100×100 numerical domain. This graph shows that the Shan–Chen algorithm successfully reproduces the Laplace–Young law. (*b*) Surface tension λ in lattice units as a function of the particle repulsion strength parameter G^{coh}.

two- or three-dimensional static problems with the Shan–Chen model can be found in several publications (see for example Huang *et al.* 2007).

The Shan–Chen model has often been favoured over other lattice Boltzmann multiphase flow models for studying flows in complex geometries (porous media) owing to its simplicity when enforcing no-slip conditions at the fluid–solid interface. Several recent studies (see for example Auzerais *et al.* 1996; Coles *et al.* 1998; Schaap *et al.* 2007; Sukop *et al.* 2008) compared their numerical calculations with digital images of natural samples obtained by X-ray tomography and found a good agreement at both the microscale (location of the fluid phases) and the macroscale (capillary pressure-saturation conditions).

3.5. *Boundary conditions*

Proper inlet–outlet boundary conditions for immiscible fluid flows have not yet been developed in the framework of the Shan–Chen method. Velocity boundary conditions for multiphase immiscible fluids are problematic, because of the dynamical coupling between both fluids through surface tension. A suitable velocity boundary condition requires a way to impose a velocity (or velocity gradient) on each fluid that does not introduce spurious effects through the viscous drag and surface tension between the two fluids. The challenge becomes even more daunting in a dynamical system where the conditions evolve at the boundary. For pressure-driven flows, injection and outlet conditions can, however, be obtained with pressure boundary conditions (Zou & He 1997).

Pressure-driven condition is a convenient assumption in many industrial applications. In nature, however, multiphase flows in porous media can also be buoyancy-driven, which is the case we focus on in this study. Our choice of boundary conditions follows Latt *et al.* (2004): the invading fluid is injected by creating a bubble inside an apposite region of the numerical domain (injection chamber). The injection of the invading fluid is performed by imposing a local density value $\sum_i f_i^{nw}$ with momentum $\sum_i f_i^{nw} \boldsymbol{v}_i$ equal to zero (bubble at rest initially). The newly created bubbles rise away from

their injection site because of their positive buoyancy (a buoyancy force is applied to the non-wetting phase only, as in (3.7)). The injection rate of non-wetting fluid is determined by the volume of each bubble and the period between successive injections. The position of the injection site, the period between injections and the volume of the bubbles can be varied over a single calculation to obtain a pseudo-random injection process.

Initially, as the injection chamber is capped by a region of low porosity (see figure 6), a layer of non-wetting fluid can form at the bottom of the low-porosity region. In this non-wetting fluid layer (see figure 6), the pressure increases until it exceeds a critical capillary pressure and the non-wetting fluid invades the porous medium (see figure 7*a*).

The injection of non-wetting fluid in the inlet chamber can, however, be prone to numerical instabilities and has to be conducted carefully. In order to avoid numerical instabilities, we use the following procedure: during the first half of the injection process, the local density of the non-wetting fluid is increased linearly with time until a fixed maximum value of density is reached. During the second half of the period of injection, the local density is kept constant. This allows us to slowly increase the magnitude of the cohesion force ((3.5); note that the magnitude of the cohesion force (3.6) is proportional to density) and slowly build up the interface of separation between the two immiscible fluids. The temperature of injected bubbles is initially at equilibrium with the temperature in the injection chamber, equal to T_0, and above the melting temperature of the fertile solid fraction.

The outlet region is located at the top of the porous medium (see figure 1). Once the non-wetting phase reaches the outlet, its density and enthalpy are absorbed exponentially over 70 nodes above the porous medium. The distance over which density and temperature are decaying and the strength of the decay (decay constant) at the outlet are set by the optimal parameters (e.g. exponential decay rate, size of outlet), where the effect of the outlet boundary is the smallest on the different field variables upstream (temperature, pore-scale velocity). These optimal parameters were found numerically.

4. Results and discussion

The injection of a non-wetting fluid phase in a saturated porous medium has been the subject of numerous studies over the last half-century. The different dynamical regimes that describe the distribution of the invading fluid phase (here non-wetting, i.e. capillary instability, viscous fingering instability and stable front propagation) are generally cast in terms of three dimensionless numbers (Lenormand *et al.* 1988; Ewing & Berkowitz 1998; Blunt 2001):

$$Ca = \frac{q_{nw}\mu_{nw}}{R^2\gamma} \quad \text{capillary number,} \tag{4.1}$$

$$Bo = \frac{\Delta\rho g R^2}{\gamma} \quad \text{Bond number,} \tag{4.2}$$

$$\lambda = \frac{\mu_{nw}}{\mu_w} \quad \text{viscosity ratio,} \tag{4.3}$$

where the indices w, nw respectively refer to the invading non-wetting and defending wetting fluids, μ is the dynamical viscosity, γ the surface tension between the two fluids, $\Delta\rho$ their density difference, q_{nw} the volume of invading fluid injected in the porous medium per unit time and R a characteristic length scale of the

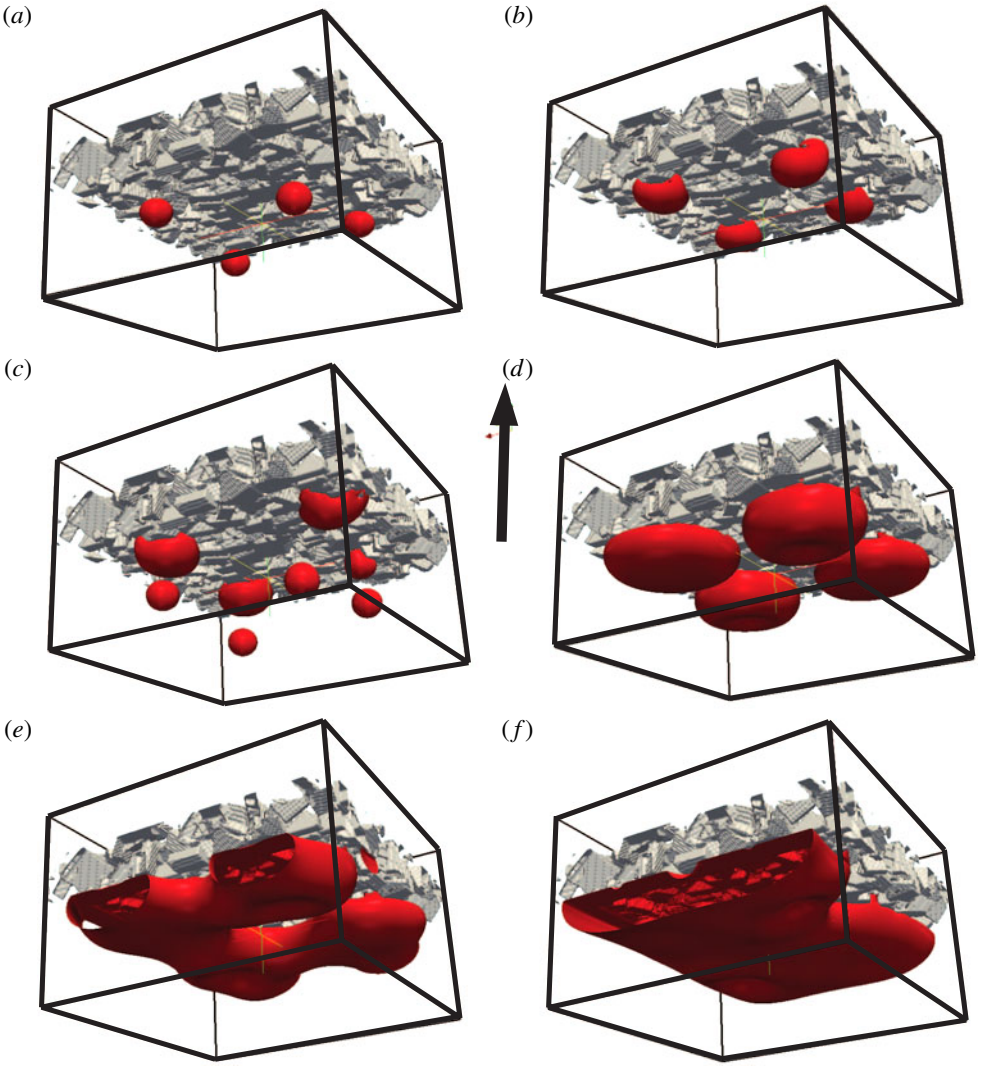

FIGURE 6. (Colour online) Bubble formation at the injection chamber. Bubbles of non-wetting fluid (density contour in red/dark grey) are periodically generated at different locations inside an inlet region. The latter is capped by the porous medium (solids fraction in light grey). The non-wetting bubbles ascend buoyantly to the bottom of the porous medium. If the permeability contrast between the inlet and the porous medium is large, bubbles coalesce and form a capillary layer of non-wetting fluid.

system, hereafter set to the average pore radius. In § 2, we showed that two more dimensionless numbers are introduced for reactive flows: the Stefan number, which gives the ratio of the amount of enthalpy associated with the dissolution/melting of the matrix to the amount of enthalpy stored in the system, and the ratio of reactant diffusivity for the two fluid phases. The following discussion applies to any type of reactive flow where the reaction is linear. To simplify the notation, we assume hereafter a thermal problem where the reactant corresponds to the excess enthalpy

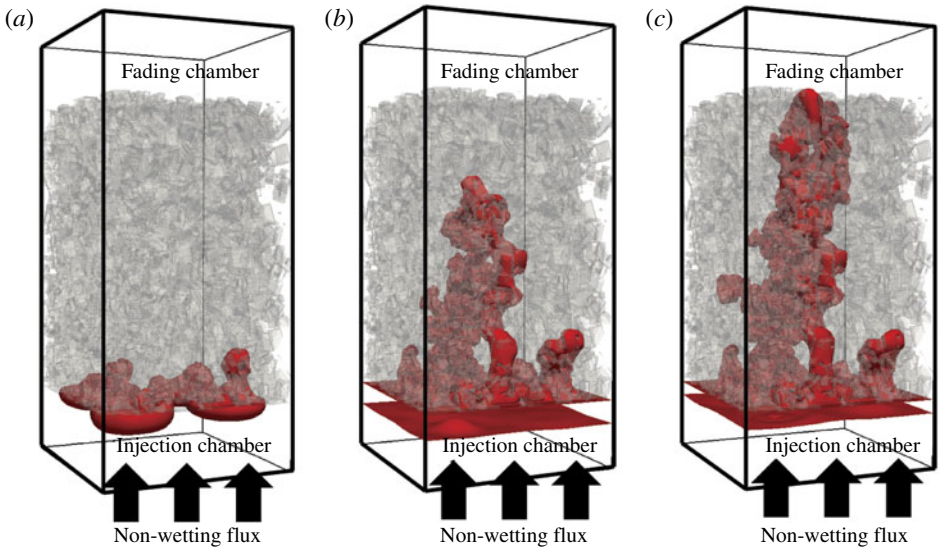

FIGURE 7. (Colour online) The porous medium, initially saturated with a wetting fluid (transparent here), is invaded by the buoyant non-wetting fluid injected at its base. The initial porosity of the porous medium is 0.41. The buoyant non-wetting fluid is depicted in red/dark grey. (*a–c*) The build-up of a capillary layer before the pressure in the stalled non-wetting-fluid exceeds a critical capillary pressure. In (*c*), we observe that the thickness of the capillary layer at the base of the porous medium decreases before reaching a quasi-steady state (for low dissolution rates) when the non-wetting phase has reached the outlet, where the non-wetting phase is absorbed with a constant rate in time.

carried by the invading phase. Thus

$$St = \frac{c\Delta T}{L_f} \quad \text{Stefan number,} \tag{4.4}$$

$$\xi = \frac{\kappa_{nw}}{\kappa_w} \quad \text{diffusivity ratio.} \tag{4.5}$$

In the definitions above, $\Delta T = T_0 - T_m$ is the temperature difference between the injected non-wetting fluid and the melting temperature of the fraction of the matrix susceptible to melting, c is the specific heat, and L_f is the latent heat of fusion. In all the calculations presented here, λ and ξ are fixed to respectively 1 and $1/7$. These values are fixed to reduce the number of free parameters in this study and to ensure numerical stability and accuracy with the present numerical method (limitation with λ). In the following section, we explore the effect of the different dimensionless numbers on the heat and mass transfer associated with the injection of a superheated invading fluid. We start with the Stefan number and discuss the importance of melting on the mass transfer of invading fluid.

4.1. *The effect of the melting/dissolution (Stefan number)*

Let us first define a stable capillary channel as a connected channel of the non-wetting phase (formed by a capillary instability) that remains connected and active for heat and mass transfer throughout the course of one of our calculations. In this section, we discuss the stability of these non-wetting fluid channels to the partial melting/dissolution of the porous matrix. We focus on the dynamics of capillary

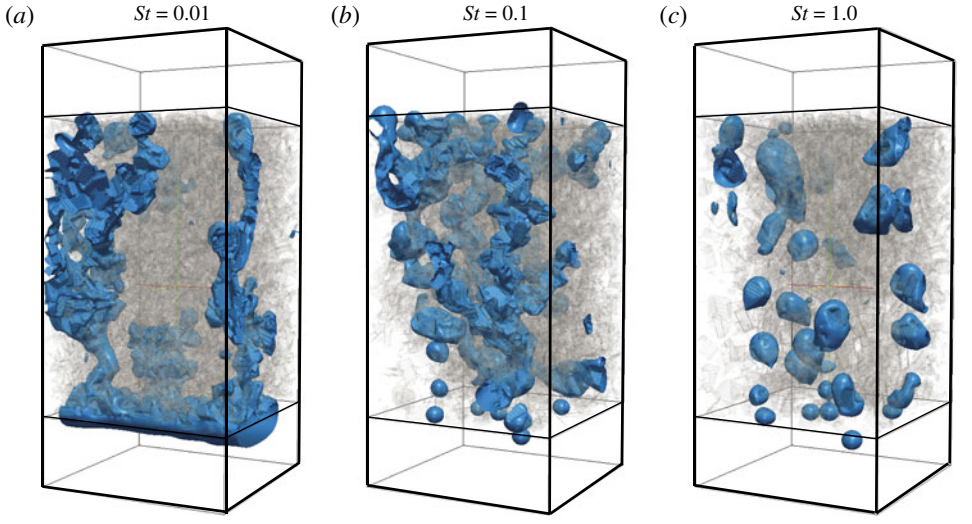

FIGURE 8. (Colour online) Comparison between the non-wetting phase distribution in three calculations with different melting efficiencies (St). At low St (a), channels of non-wetting fluid are well-defined and stable. As the melting efficiency increases (increasing St), channels become less stable (b, c) and eventually break into slugs or bubbles. Note in transparency the decrease in crystallinity (increase in porosity) in the lower part of the texture because of melting.

channels as they control the heat transfer beyond the melting front associated with heat diffusion and host the majority of the mass transport of non-wetting fluid through the porous matrix.

Although elongated channels of fluid embedded in an unbounded and immiscible viscous or inviscid ambient fluid have been shown to be unstable to capillary forces (see for example Newhouse & Pozrikidis 1992; Eggers 1993; Papageorgiou 1995; Chen & Steen 1997; Day, Hinch & Lister 1998; Zhang & Lister 1999; Sierou & Lister 2003; Quan & Hua 2008), the effect of confining solid boundaries and steady flow through the channel have been suggested to slow down the breakup of the channel into bubbles or slugs (Tomotika 1935; Hagedorn *et al.* 2004). In a dynamical setting such as when capillary channels invade a porous medium, however, these structures are known to be able to remain stable over the duration of laboratory or numerical experiments as long as the injection rate of the invading fluid remains constant. One could therefore argue that the confinement of the two fluid phases in a porous medium and a steady injection rate of invading fluid that can sustain a high local saturation of invading fluid in the channel are able to stabilize the channel at least over much greater time scales.

The topology of the porous medium, and therefore of the buoyancy-driven capillary channels of non-wetting fluid, are complex (see figure 13). Our calculations clearly show the influence of the Stefan number on the stability of channels (figure 8). In order to better understand qualitatively the role of melting/dissolution in the dynamics of the invading fluid, we assume a much simpler conceptual model where the non-wetting phase occupies a perfect cylindrical channel at the centre of a cylindrical tube wetted by the other fluid (axisymmetrical annular flow). Figure 9(a) shows the simplified geometry in two dimensions, and defines some useful notation. We first assume a multiphase axisymmetrical flow with constant radius R_g (radius of the

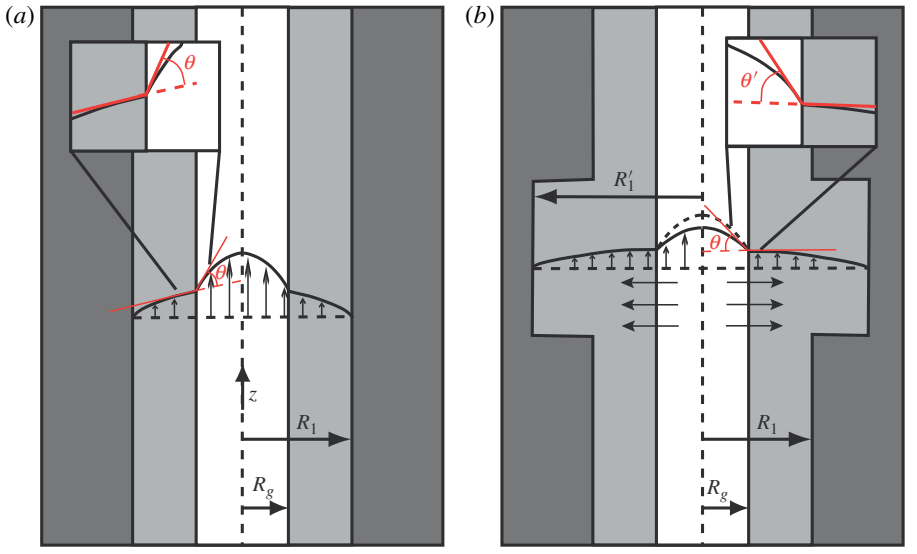

FIGURE 9. (Colour online) Conceptual model of axisymmetrical annular flow. (*a*) The steady-state flow expected when the channel as a constant radius. In (*b*) we see that, when a section of the channel is wider ($R_1' > R_1$), mass conservation imposes that the flow is slowed down in the wider region (see (4.11)). The varying radius introduces curvature at the interface between the non-wetting and wetting fluids and, together with the longitudinal stretching of the channel above the wider region, destabilizes the channel. See the text for more details.

non-wetting fluid) and R_1 for the wetting fluid. The solution to this annular flow is

$$u(r) = \begin{cases} -\dfrac{1}{4\mu_w}\dfrac{\mathrm{d}p}{\mathrm{d}z}(R_1^2 - r^2) & R_g \leqslant r \leqslant R_1, \\ -\dfrac{1}{4\mu_{nw}}\dfrac{\mathrm{d}p}{\mathrm{d}z}(R_g^2 - r^2) - \dfrac{1}{4\mu_w}\dfrac{\mathrm{d}p}{\mathrm{d}z}(R_1^2 - R_g^2) & 0 \leqslant r \leqslant R_g, \end{cases} \tag{4.6}$$

where z is the direction along the axis of the cylinder, $\mathrm{d}p/\mathrm{d}z$ is the dynamical pressure gradient causing the flow and μ_{nw}, μ_w are respectively the viscosity of the non-wetting and wetting fluid. The angle θ between the velocity gradient in the radial direction at R_g is related to the viscosity ratio λ,

$$\theta = \operatorname{atan}\left(\left.\frac{\mathrm{d}u}{\mathrm{d}r}\right|_{R_g^+}\right) - \operatorname{atan}\left(\left.\frac{\mathrm{d}u}{\mathrm{d}r}\right|_{R_g^+}\frac{1}{\lambda}\right), \tag{4.7}$$

where $\lambda = \mu_{nw}/\mu_w$ and R_g^+ is the limit $R_g + \epsilon > R_g$ for $\epsilon \to 0$.

In order to see how the non-wetting fluid channel behaves when a section of the confining solid is subjected to melting, we assume that the radius R_1 is perturbed to a new radius $R_1' > R_1$ over a depth Δz. To simplify the discussion, we assume that only a small subregion of the channel was affected by melting (because of heterogeneous solid melting temperatures for example, as in our more realistic calculations) and that the axisymmetry is conserved. Moreover, we will assume that the region Δz over which melting increased $R_1 \to R_1' > R_1$ is deep compared to the depth over which the gradients $\mathrm{d}R_1'/\mathrm{d}z$ are significant and that a Hagen–Poiseuille flow can approximate the flow solution in Δz far away from the boundary of Δz. In this case, at steady state, the

solution for the flow within Δz is

$$u'(r) = \begin{cases} -\dfrac{1}{4\mu_w}\dfrac{\mathrm{d}p'}{\mathrm{d}z}(R_1'^2 - r^2) & R_g' \leqslant r \leqslant R_1', \\ -\dfrac{1}{4\mu_{nw}}\dfrac{\mathrm{d}p'}{\mathrm{d}z}(R_g'^2 - r^2) - \dfrac{1}{4\mu_w}\dfrac{\mathrm{d}p'}{\mathrm{d}z}(R_1'^2 - R_g'^2) & 0 \leqslant r \leqslant R_g', \end{cases} \tag{4.8}$$

where the prime denotes variables that have been perturbed by a melting event that lead to the new configuration shown in figure 9(*b*). After melting, mass conservation for both fluids requires that

$$q_w = \pi \int_{R_g}^{R_1} u(r) r \,\mathrm{d}r = \pi \int_{R_g'}^{R_1'} u'(r) r \,\mathrm{d}r, \tag{4.9}$$

$$q_{nw} = \pi \int_{0}^{R_g} u(r) r \,\mathrm{d}r = \pi \int_{0}^{R_g'} u'(r) r \,\mathrm{d}r. \tag{4.10}$$

We can therefore solve for the new pressure drop $\mathrm{d}p'/\mathrm{d}z$ and non-wetting channel radius R_g' as a function of the change in radius due to melting $R_1 \to R_1'$. The non-wetting channel radius in the wider part of the conduit is then given by

$$R_g' = \sqrt{\frac{\sqrt{4AC + B^2}}{2A} - \frac{B}{2A}}, \tag{4.11}$$

where

$$A = R_1^2 \left[2\left(\frac{1}{4} - \frac{\lambda}{2}\right)(R_1^2 - R_g^2) - \frac{\lambda}{2} R_g^2 \right], \tag{4.12}$$

$$B = R_1'^2 \left[R_g^4 \left(\frac{1}{2} - \frac{\lambda}{2}\right) + \lambda R_1^4 \right], \tag{4.13}$$

$$C = 2R_1'^4 \left[R_g^4 \left(\frac{1}{4} - \frac{\lambda}{2}\right) + \frac{\lambda}{2} R_1^2 R_g^2 \right]. \tag{4.14}$$

Figure 10 illustrates the dependence of the capillary channel radius in the wider conduit (R_g') as a function of the change in conduit radius R_1'. For $R_1' > R_1$, the channel becomes wider ($R_g' > R_g$). This results from the fact that melting pushes the no-slip boundary at R_1 further away and therefore decreases the shear stress at the boundary when $R_1' - R_g' > R_1 - R_g$.

As $q_{nw} \propto U_{nw} R_g^2$, where U_{nw} is the average velocity of the non-wetting phase in the capillary channel, we expect that the average flow velocity in the wider region is decreased by a factor $(R_g/R_g')^2$. This induces longitudinal gradients of velocity $\partial u/\partial z$ in the vicinity of Δz, where the flow is slowed down when the non-wetting phase approaches the widening of the conduit. It leads to an accumulation of non-wetting fluid. The stretching of the channel above the wider region and the longitudinal perturbation of radius R_g with z around Δz are expected to favour capillary instabilities (such as Rayleigh–Plateau instabilities) that can cause the breakup of the channel into slugs or bubbles of non-wetting fluid. We tested this conceptual model with a numerical calculation, where the temperature of the non-wetting fluid is raised instantaneously in an axisymmetric annular flow after a steady-state flow is reached. The solid walls are constructed similarly to the conceptual model (figure 9), where only a narrow band at the centre is allowed to melt. In figure 11, we observe that

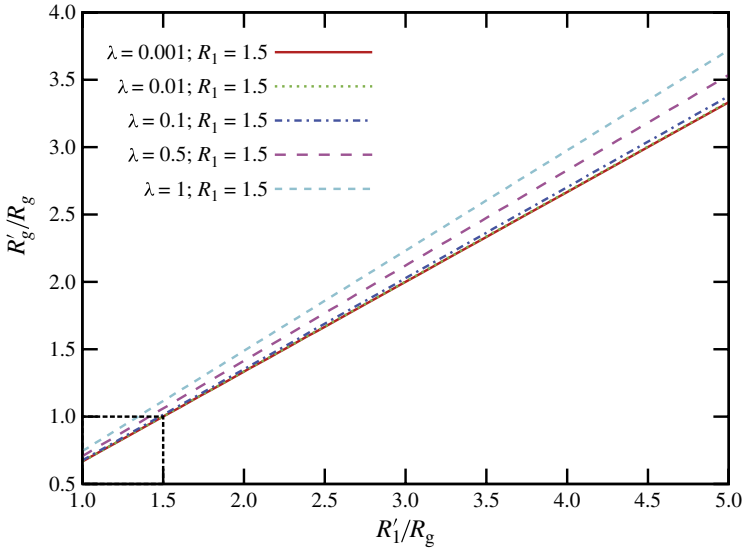

FIGURE 10. (Colour online) Results from the simplified analytical axisymmetric annular flow model shown in figure 9. The results illustrate how the non-wetting fluid channel adjusts (after reaching a new steady state) to a change in radius R_1 for different values of viscosity ratio λ.

only a small amount of melting (∼1 %) is required for instability (oscillations at the interface between the two fluids) and leads to the breakup of the capillary channel.

In all calculations, the injection rate of buoyant non-wetting fluid remains constant during a single run. The local increase in porosity associated with melting directly affects the local non-wetting phase saturation S_{nw},

$$\frac{\mathrm{d}S_{nw}}{\mathrm{d}t} = \frac{1}{V\phi^{(0)}}\frac{\mathrm{d}V_{nw}}{\mathrm{d}t} - \frac{V_{nw}^{(0)}}{V\phi^{(0)2}}\frac{\mathrm{d}\phi}{\mathrm{d}t}, \tag{4.15}$$

where the superscript 0 refers to an initial condition, V is the reference volume of porous medium, V_{nw} is the volume of non-wetting fluid in V and ϕ is the porosity. Equation (4.15) shows that when the increase of volume of non-wetting fluid induced by the longitudinal reduction of flow velocity associated with melting does not keep up with the porosity increase, the local saturation of non-wetting fluid decreases, the capillary channel is unstable and eventually breaks. The two time derivatives in (4.15) introduce two competing time scales, $\tau_{nw} \sim \Delta z[(R_g'^2 - R_g^2)/R_g^2]/U_{nw}$ for the volume change of non-wetting fluid and a time scale for the porosity evolution (melting) $\tau_m \sim R_1^2/(\zeta^2(St)\kappa_{eff})$. In the definition of τ_m, $\zeta(St)$ is an implicit and monotonically increasing function of St (see (4.20)) and κ_{eff} is a multiphase radial thermal diffusivity. For an axisymmetric annular flow, assuming a temperature drop across the pipe radius R_1 of $\Delta T = \Delta T_{nw} + \Delta T_w$, we get

$$k_{nw}\frac{\Delta T_{nw}}{R_g} \sim k_w\frac{\Delta T_w}{R_1 - R_g}, \tag{4.16}$$

where k_i is the thermal conductivity of phase i and ΔT_i is the radial temperature drop in the fluid i. The effective multiphase thermal diffusivity in this simplified geometry

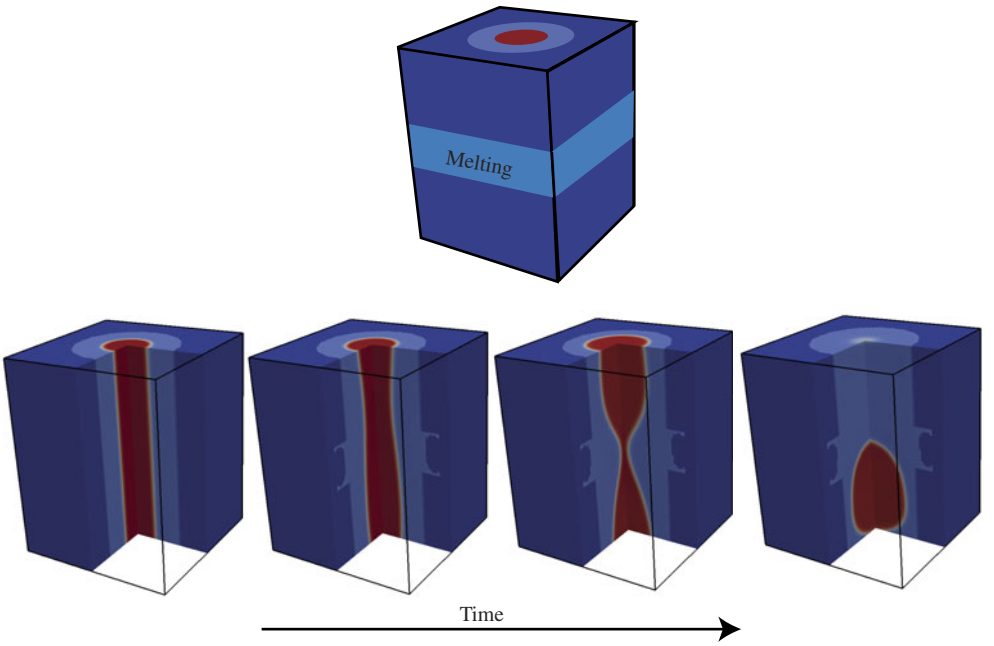

FIGURE 11. (Colour online) Snapshots of a calculation where an axisymmetric annular flow ($S_{nw} = 0.27$) is initially at steady state. The boundary conditions are periodic. The solid walls (in blue/outer dark layer) bounding the annular flow are made of the refractory solid fraction (no melting possible) except for a narrow band at the centre of the conduit where the solid can melt. After reaching a steady state, the temperature of the non-wetting fluid (in red/darkest, most central shading) is instantaneously raised above the melting temperature of the centre band of fertile solid. As soon as melting occurs, a Rayleigh–Plateau instability is initiated (the capillary channel oscillates), which leads to the breakup of the channel. The amount of melting necessary to disrupt the channel was found to be only 1 % of the original sample volume.

becomes

$$\kappa_{eff} \sim \kappa_{nw} \left(1 - \frac{\Delta T_w}{\Delta T}\right) \frac{R_1}{R_g}, \tag{4.17}$$

where ΔT_w is given by

$$\Delta T_w \sim \frac{\kappa_{nw} c_{nw} \rho_{nw} \Delta T (R_1 - R_g)}{\kappa_w \rho_w c_w R_g + \kappa_{nw} c_{nw} \rho_{nw} (R_1 - R_g)}. \tag{4.18}$$

If the $\tau_m < \tau_{nw}$, i.e. the Stefan number is large or the injection rate is small, melting is expected to reduce the local saturation of the non-wetting phase, which at some point will lead to the breakup of the capillary channel; on the other hand, if $\tau_m > \tau_{nw}$, then S_{nw} decreases only slowly and the channel remains stable for a longer duration.

Our discussion of the effect of melting on the breakup of capillary channels in porous media has been limited so far to isochoric (no volume change) phase changes during melting. Most substances (except, for example, water) exhibit a volume increase upon melting. In this particular case, we hypothesize that the volume increase associated with the phase change will promote the destabilization of the channel as the local overpressure is expected to accelerate the pinch-off process.

4.2. *Injection rate, capillary number*

Lenormand *et al.* (1988), Ewing & Berkowitz (1998) and Blunt (2001) discussed the importance of the injection rate of an invading fluid in the generation of capillary or viscous fingering instabilities. They showed that for viscosity ratios close to unity ($\lambda \sim 1$), corresponding to our calculations, instabilities originate from capillary effects as long as the injection rate or Ca does not exceed a value of $\sim$1. Our calculations are set with a fixed viscosity ratio $\lambda = 1$, a fixed Bond number $Bo \sim 0.1$ and over a range of capillary numbers $Ca \sim 10^{-4} - 10^{-1}$, where the latter two numbers use the initial average pore radius as the reference length scale. A major difference between our calculations and typical capillary instabilities lies in the fact that, in a melting environment, the dimensionless numbers St, Bo and Ca are evolving with time because (i) the non-wetting phase loses heat to the wetting fluid and to melt the porous matrix, and (ii) the average pore radius evolves with time as a result of melting. In this section we briefly discuss how melting affects Ca.

A time-dependent definition of the capillary number for the injection of the invading fluid includes the evolution of the average radius size of the relevant pores, which are bound to increase because of melting. Using the same model as above, where the multiphase flow through the porous medium is simplified to an annular flow through a vertical pipe, we assume that melting increases the radius of the pipe at a certain level of the porous media according to

$$R_1(t) = R_1^{(0)} + 2\zeta\sqrt{\kappa_{eff} t}. \tag{4.19}$$

Assuming a simplified heat transfer problem in a cylinder (Carslaw & Jager 1959), ζ becomes

$$\zeta^2 \exp(\zeta)\mathrm{Ei}(-\zeta^2) + St = 0, \tag{4.20}$$

where Ei is the integral exponential function. Figure 12(*a*) shows the evolution of Ca versus time (normalized using the Fourier number $Fo \equiv \kappa_{eff} t/R_1^2$) for different St for this idealized melting problem. Figure 12(*a*) illustrates that, although the injection rates of non-wetting fluid q_{nw} remain constant for each calculation, Ca decreases faster for greater St. In the pore-network calculations of Lenormand *et al.* (1988), the invading fluid flows in response to the injection rate solely (no buoyancy) and capillary instabilities percolate through the porous medium as long as Ca remains finite. For buoyant flows, however, the situation is different. If the mass flow rate of the buoyant non-wetting phase locally exceeds the injection rate (which is possible at low Ca or high Bo), capillary channels can break into slugs disconnected from the injection region.

We conducted calculations with various injection rate values, and hence Ca, for fixed $Bo = 0.1$, (i) to test if capillary channels were able to grow, and (ii) to measure the characteristic non-wetting fluid velocity (defined as $\sim$1/2 of the maximum velocity) in the main capillary channel. The results are summarized in figure 12(*b*). We see that below a given value of injection rate, corresponding here to a critical $Ca_{cr} \sim 3 \times 10^{-3}$, the non-wetting phase rises through the porous medium as disconnected slugs or bubbles. All the calculations reported in the next sections have been performed with an initial $Ca > Ca_{cr}$ in order to observe the dynamics of capillary channels; however, as discussed above (see figure 12*a*), Ca decreases with time because of melting. We note that the simple Ca evolution trends shown in figure 12 assume a constant St, which is an obvious overestimate of the evolution of the melting efficiency as the superheat in the non-wetting phase decreases with time

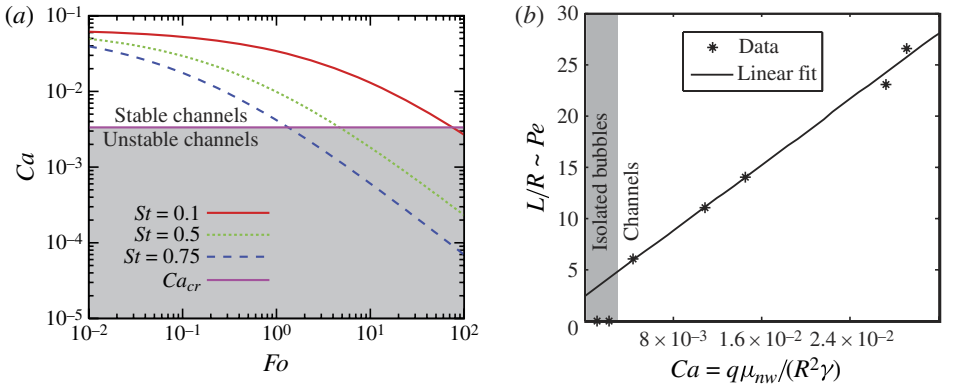

FIGURE 12. (Colour online) Simplified temporal (dimensionless: see text) evolution of the capillary number Ca for the non-wetting fluid injection (a). Ca is expected to decrease with time even for constant injection rate because of its dependence on the channel radius (the radius increases because of melting). The rate of Ca decrease is controlled by the Stefan number St (see (4.20)). As Ca decreases, the non-wetting fluid saturation S_{nw} decreases (at constant injection rate) and channels are no longer stable. The threshold value here is obtained from calculations where we vary the injection rate at constant Bond and Stefan numbers. Melting (St) and buoyancy (Bo) start to prevent the growth of connected channels in the porous medium if the injection rate or Ca becomes to small (b). The vertical axis in (b) represents the aspect ratio of isothermal contours in non-wetting fluid channels (set at a dimensionless temperature of 0.1, 0 = melting temperature and 1 = injected non-wetting fluid temperature).

and distance away from the injection point (due to heat absorbed by the wetting fluid and the solid matrix).

To summarize, the competition between the injection rate of non-wetting buoyant fluid (Ca), buoyancy (Bo) and superheat (St) controls the stability of capillary channels during our calculations. We observe that for large amounts of superheat or large buoyancy and small injection rates, channels can be destabilized and break into slugs under the action of capillary forces. Moreover, the dimensionless numbers describing the balance between injection of non-wetting fluid, buoyancy and capillary forces vary temporally and spatially because of localized melting. For instance, Ca decreases with time locally because of the evolution of the channel radius with melting. The superheat carried by the non-wetting phase (which is responsible for melting deep in the porous medium) is gradually absorbed by the surrounding melt and the latent heat of the matrix. As a result, the melting efficiency (St) decreases with time and also with distance from the injection region. At large St, we observe (figure 8) that melting inhibits the formation and stability of capillary channels; however, as time progresses and at greater distance from the lower boundary (injection region), St is significantly reduced and a situation similar to low St number regimes (growth of long-lasting capillary channels) is recovered. This observation encourages us to focus on calculations at intermediate-to-low St (<1), where capillary instabilities control the heat and mass flux associated with the invading fluid, because they are also consistent with the mode of heat and mass transfer at higher melting efficiencies beyond a small buffer region (a few pore radii above the injection region in our calculations) where melting absorbs most of the superheat.

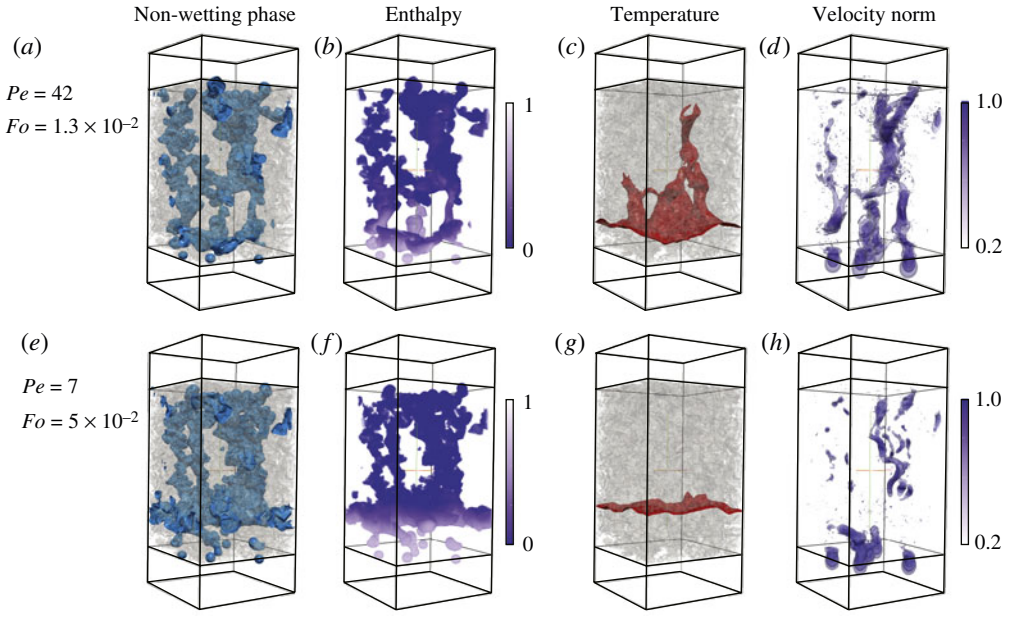

FIGURE 13. (Colour online) Comparison of two calculations at $St = 0.1$ with different local Pe values (local here refers to the Péclet number measured in the main capillary channel: see text for clarifications). We show (a) density contours for the non-wetting fluid, (b) the normalized excess enthalpy carried by the buoyant non-wetting fluid, (c) an isotherm (at 0.1) and (d) the normalized velocity magnitude of the non-wetting fluid. We observe that, for $Pe = 7$, the melting front is more localized to the region where the front propagates by diffusion from the inlet region, whereas, for $Pe = 42$, the heat transfer penetrates deeper into the porous medium.

4.3. *Reactant transport*

In this section, we discuss the non-wetting fluid mass and associated heat transport in capillary channels. We define a local Péclet number to quantify the ratio of advective to diffusive reactant/heat transport in capillary channels,

$$Pe = \frac{u_{l,nw} R_l}{\kappa_{eff}}, \tag{4.21}$$

where the subscript l refers to local, i.e pore-scale definitions, R_l is a characteristic pore radius in the capillary channel, $u_{l,nw}$ is a characteristic non-wetting phase flow velocity in the channel (usually $\sim$50 % of the maximum velocity). We emphasize that this definition of the Péclet number measures the relative contribution of reactant transport in capillary channels at the pore scale, and, as such, is not a direct macroscale measure of the reactant/heat transport in the porous medium. Figure 13 illustrates typical results with snapshots showing the distribution of mass, excess enthalpy, temperature (isotherm contour $(T - T_m)/T_m = 0.1$) and velocity magnitude we obtain at low Stefan number ($St = 0.1$). The two rows allow us to compare visually the behaviour of our results for two different local Péclet numbers.

In order to quantify the penetration of non-wetting phase and heat in the porous medium vertically from the injection region (inlet), we discretize the porous medium in N (generally using $N = 6$) equal-sized horizontal sections (see figure 14a). The number of sections (N), and therefore the thickness of each layer (50 calculations

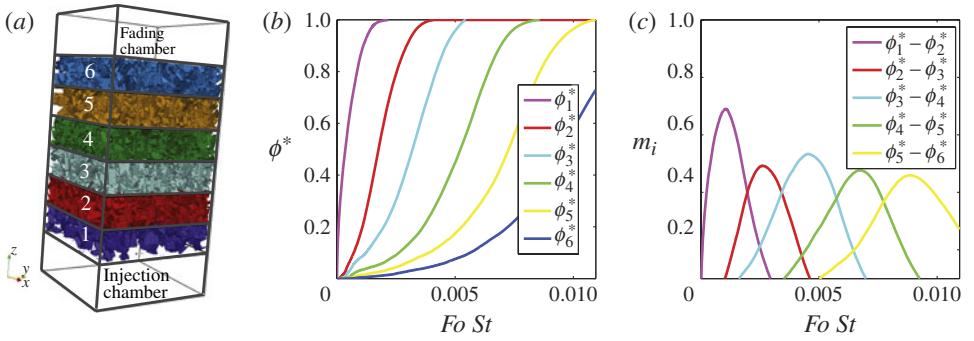

FIGURE 14. (Colour online) The porous medium is sliced into N (here $N = 6$) layers to better track the temporal and spatial evolution of the melting front in the porous medium (*a*). (*b*) An example of normalized porosity evolution (defined in (4.22)) for the different layers, where time is made dimensionless using the thermal diffusion (for non-wetting phase) time scale. (*c*) Temporal evolution of m_i defined in (4.23). These functions allow us to track the migration of the melting front and to assess the depth of penetration of the heat transfer into the porous medium as a function of time.

point along the vertical dimension for $N = 6$) is chosen to be large enough to provide robust statistics about the temporal evolution of the average porosity and gas saturation in each layer and small enough to gain a better understanding of the vertical distribution of melting and gas transport. Because of the random distribution of grains/crystals with a melting temperature greater than the maximum temperature of the system (corresponding to $\sim$21 % of the volume of the sample), each layer is expected to have a different amount of these refractory phases (see figure 2). To compare the amount of melting in each layer, we normalize the porosity to

$$\phi^*(z_i, t) = \frac{\phi(z_i, t) - \phi_{min,i}}{\phi_{max,i} - \phi_{min,i}}, \tag{4.22}$$

where z_i references the position of the layer ($z_i = 1, 2, 3, \ldots, N$ from the lowest to the top layer), $\phi_{min,i}$ and $\phi_{max,i}$ are respectively the initial and maximum porosity (1-refractory phase fraction) of the layer (figure 14*b*).

One would expect that at low Pe, when heat transfer is dominated by diffusion from the inlet region, melting would be, at least at early times ($t \ll (N * \mathrm{d}z)^2/\kappa_{eff}$, where $\mathrm{d}z$ is the distance between z_i and z_{i-1}), confined only to the lower layers. In contrast, at high Pe, when channels of non-wetting fluid are developed, the penetration depth of heat and melting in the porous medium is expected to grow with increasing Pe. To compare the contemporary evolution of the porosity in each layer and assess the localization of melting vertically, we introduce

$$m_i(t) = (\phi^*(z_i, t) - \phi^*(z_{i+1}, t)). \tag{4.23}$$

The m_i are generally positive functions which initially grow as the lower layer of the pair (i) experiences initially more melting. They reach a maximum when the melting rate of the two layer is comparable and finally decrease monotonically once the melting front is shifted upwards (higher than position z_i): see figure 14(*c*). The height of the maximum of m_i is controlled by the duration over which melting is dominantly occurring in the layer i and only marginally in $i + 1$ and therefore can be used to quantify the amount of vertical localization of the region over which melting occurs. As the most rapid melting occurs initially in the lowermost layer, when the superheat

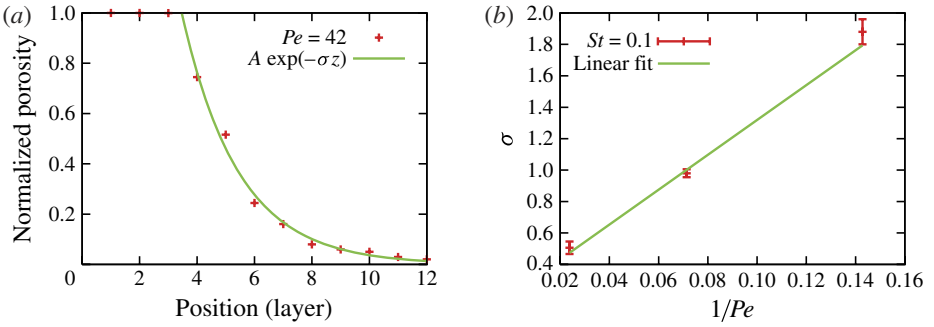

FIGURE 15. (Colour online) (*a*) Comparison of a melting profile from our calculations with the simple scaling law of (4.27). Panel (*b*) shows that the argument of the exponential melting decay with depth σ is proportional to Pe, as expected from the scalings.

carried by the non-wetting phase is maximal and the porous medium remains fertile to melting, the maximum values of $m_i(t)$, $\max(m_i)$, are expected to decrease away from the inlet region (with increasing i) with a few exceptions due to the actual distribution of refractory solids in each layer.

Assuming again a simple geometry consisting of a cylindrical pipe of radius R with fixed wall temperature (here corresponding to the melting temperature of the fertile solid fraction T_m), and a steady fluid flow entering at temperature $T_0 > T_m$ but neglecting the effect of melting (latent heat absorbed and changes in pipe radius), the mid-point (i.e. $r = 0$) temperature distribution along the pipe T_z is given by (Bejan 2004)

$$T_z(z) = T_m + (T_0 - T_m)\exp[-\sigma(z - z_0)], \tag{4.24}$$

where z_0 is the inlet region of the pipe and $\sigma = A/(RPe)$ with $Pe = uR/\kappa$ and A is a constant. We approximate the radial heat transfer out of the pipe with

$$q_r(z) \sim -k_{eff}\left(\frac{T_z(z) - T_m}{R}\right). \tag{4.25}$$

Assuming that the pipe wall is able to melt, and that the melting rate is low (limit of low St), the heat flux balance at the wall determines the melting rate at the wall,

$$q_r(z) \sim \rho_s L_f R\frac{\mathrm{d}\phi}{\mathrm{d}t}, \tag{4.26}$$

and hence, for small St in a simplified pipe flow geometry, we should expect the amount melting to decrease exponentially along the pipe,

$$\phi(z > z_0) \sim \phi(z = z_0)\exp(-\sigma z), \tag{4.27}$$

where $\sigma \sim 1/Pe$. Figure 15(*a*) shows an example of a porosity profile (averaged over each of the horizontal layers) for a calculation with initially $St = 0.1$ compared with a fit of the form $\exp(-\sigma z)$. We plot in figure 15(*b*) the dependence of the fitting constant σ on Pe for three different Pe at $St = 0.1$. These results are in good agreement with the expected results for axisymmetric pipe flows in the limit of $St \ll 1$; even if the geometry of the conduit in our calculations is much more complex, the flow is multiphase and the porous medium has a heterogenous distribution of fertile and refractory grains. This analysis reveals that, for $St \ll 1$, the heat can be channelled

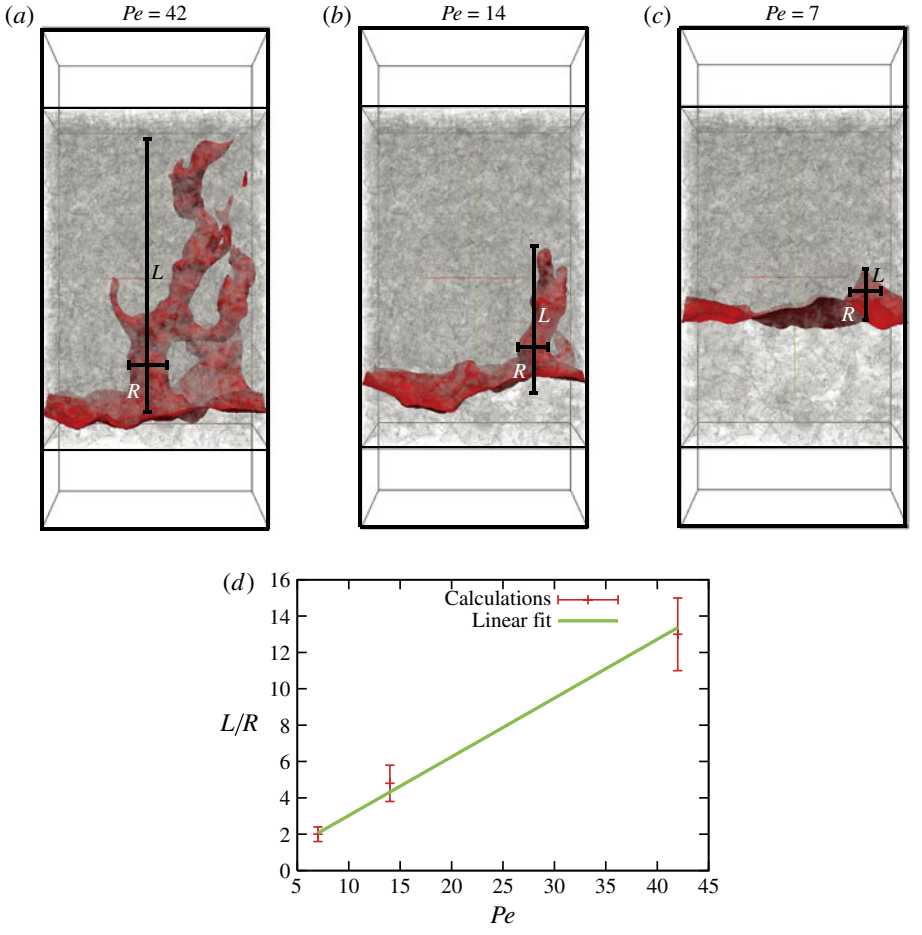

FIGURE 16. (Colour online) Snapshots illustrating the dependence of the aspect ratio L/R of isotherms in the channels on the local Pe. Panel (d) suggests that the aspect ratio L/R is linearly proportional to Pe. The error bars are calculated from the spatial resolution of our calculation.

vertically through the porous media ahead of the inlet over a penetration distance that scales like Pe. For $Pe \ll 1$, the heat transfer to the wetting fluid and solid matrix becomes predominantly radial around the main capillary channels rather than vertical from a sub-horizontal melting front migrating upwards from the inlet.

Another way to approach the characterization of the heat penetration depth L in a capillary channel of radius R is readily done by using the average non-wetting fluid velocity in the channel $\boldsymbol{u}_{nw}$ and the characteristic time scale for heat loss radially by diffusion $\tau \sim R^2/\kappa_{eff}$:

$$\frac{L}{R} \sim \frac{\boldsymbol{u}_{nw}\tau}{R} = Pe. \tag{4.28}$$

Figures 16(*a*)–16(*c*) illustrate the dependence of L on Pe; the aspect ratio of the thermal contours in the capillary channels are plotted against Pe in figure 16(*d*).

The scaling relationship of (4.28) predicts that, as long as the St number is $\ll 1$, the aspect ratio of the thermal contours in the capillary channels depends linearly on Pe.

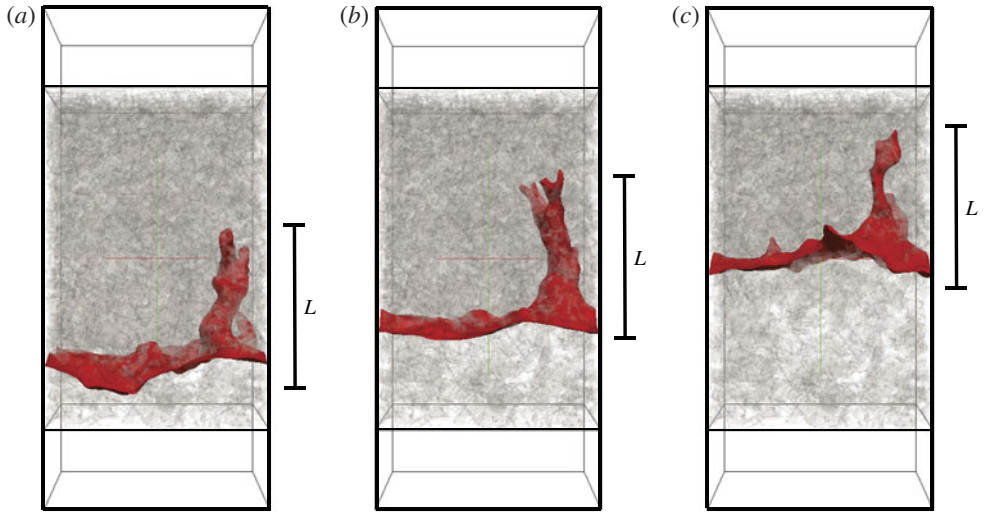

FIGURE 17. (Colour online) Snapshots of calculations at $Pe = 14$, $St = 0.1$ taken at different times. They show that, for low St, the aspect ratio of isotherms in capillary channels remains approximately constant with time.

The scaling remains valid and the aspect ratio approximately constant as long as the flow and the channel width remain roughly constant with time (see figure 17).

Further useful information on the heat transfer associated with the flux of buoyant superheated non-wetting fluid can be extracted from the maximum values of m_i for each layers: the migration rate of the melting front. We define t_i as the time in our calculations when m_i reaches its maximum value. We expect that at $Pe \gg 1$ the heat transfer is dominated by the advective flux associated with capillary channels, which remains mostly constant during our calculations (see figure 17). In the following figures, time is made dimensionless using the Fourier number $Fo = \kappa_{nw} t/R^2$, where R is the average pore radius in the capillary channel. At $Pe \gg 1$, the relationship between t_i and z_i is expected to be linear (see figure 18*a*,*d*,*e*) with a slope β proportional to $1/Pe$ (figure 18*b*,*c*). In contrast, at lower values of Pe ($\leqslant O(1)$), the heat transfer is dominated by diffusion from the inlet region and the power-law exponent $t_i \sim z_i^{\zeta}$, where ζ is expected to approach the limit $\zeta = 2$ when $Pe \to 0$ (figure 18*d*,*e*). We also compare the migration of the melting front for different initial values of St, from 0.1 to 1. We observe that the migration rates are significantly different even for similar Pe. However, if we rescale the time with St to account for the effect of melting on the heat transfer (figure 18*b*), the migration rate becomes much more comparable over the range of St at fixed Pe. The residual variability in the dimensionless migration rate at a given Pe across the range of St can be explained by the presence, at high St, of a largely melted buffer region next to the inlet where the initial superheat is partially absorbed before capillary channels are stabilized.

4.4. *Macroscale evolution*

In this section, we discuss the evolution of the system at the scale of the porous media sample. We focus on the evolution of two scalar fields: (i) the overall normalized porosity, and (ii) the non-wetting fluid saturation (pore volume fraction). Because the dynamics at high St (close to unity) is transient and evolves to $St \ll 1$ after a buffer layer of a few average pore radii absorbs most of the superheat of the non-

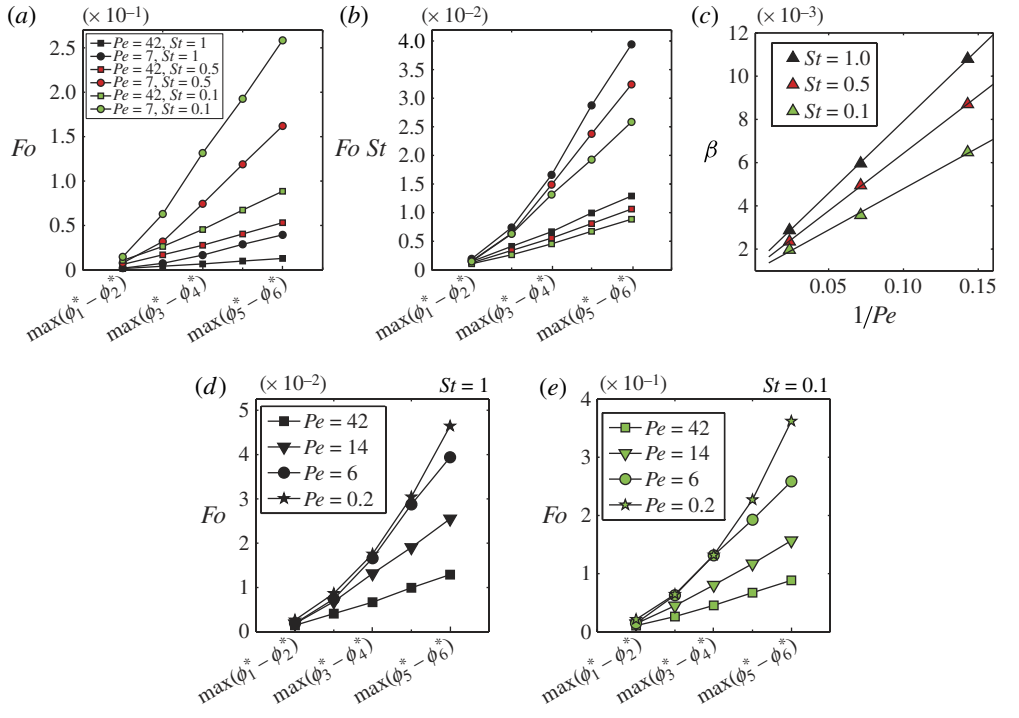

FIGURE 18. (Colour online) Using the time (dimensionless) at which the functions m_i reach a maximum, we can track the migration of the melting front. We observe (i) that St exerts a strong influence on the front migration (see (a)), but, when the time is rescaled with St, results from different St calculations and identical Pe become comparable. At low Pe, melting is dominated by heat diffusion from the inlet (see migration rate $\sim Fo^{1/2}$ in (d)–(e) instead of $\sim Fo$). Panel (c) shows the dependence of the slope of the trends in (a) on Pe for different St. The slope satisfies $\beta \sim 1/Pe$, as expected.

wetting fluid, we centre the discussion on lower St ($St = 0.1$). Figure 19(a) shows the normalized porosity increasing with dimensionless time in response to the amount of superheat injected with the non-wetting fluid in the porous medium. We observe that even for $Pe > 1$, at early times (small Fo), diffusive heat transfer from the inlet region dominates and the $\phi^* \sim Fo^{1/2}$. As soon as capillary channels develop and melting moves away from the inlet region, we observe a transition to a linear relationship $\phi^* \sim Fo$ characteristic of a heat transfer dominated by advection. However, one can easily observe that the slope of $\phi^*(Fo)$ does not depend linearly on Pe, contrary to our discussion in the preceding section. This is because our definition of Pe is local (pore scale) and does not apply to an effective Pe at the Darcy scale. The latter is of limited use because the macroscale evolution of the system is strongly correlated to pore-scale processes (capillary instabilities, reactive transport).

Figure 19(b) shows the evolution of the global non-wetting phase saturation in the porous medium as a function of time (Fo). First, the saturation builds up as the non-wetting phase accumulates. Second, the increase in porosity associated with melting contributes negatively to S_{nw} because $S_{nw} \sim 1/\phi^*$. The two regimes observed in the saturation evolution reflect the two competing processes, (i) injection of non-wetting phase on the positive side, and (ii) melting on the negative side. A steady state was

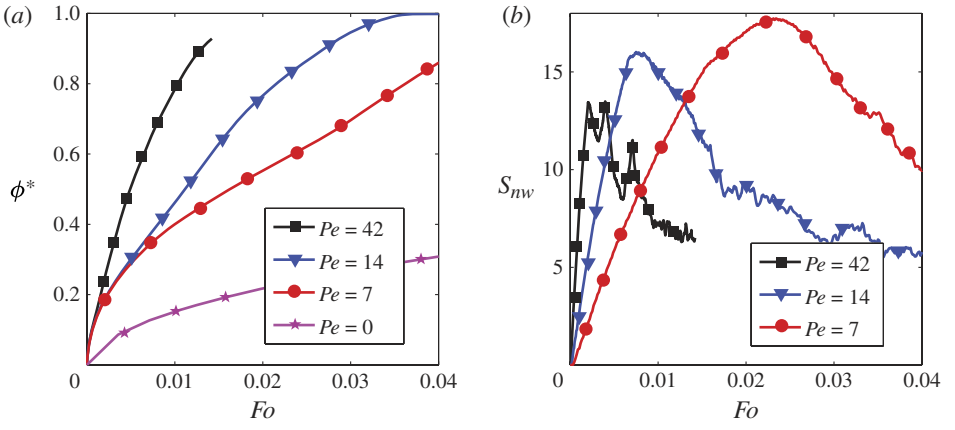

FIGURE 19. (Colour online) Overall evolution of the porous medium for $St = 0.1$ and various local Pe. (*a*) The melting rate is greater for greater Pe, as expected. (*b*) Evolution of the overall non-wetting phase saturation S_{nw}. Early on the saturation increases because of the injection; it then reaches a maximum and decreases because of melting (increase in porosity).

not found during our calculations because of limited computational resources and the time required to melt the solid matrix far away from the inlet and from superheated channels.

Our calculations highlight the importance of localized transport of mass and reactant in capillary channels during the invasion of a buoyant non-wetting fluid in porous media. The viability of these capillary channels is increased when the ratio of mass transport of non-wetting fluid to superheat is maximized.

5. Conclusion

Multiphase flows in porous media control to a great extent the mass, heat and chemical balance in the vadose region. In some instances, reactants are transported by one of the two fluid phases and influence the mass transfer when reactions affect the flow pathways at the pore scale. The coupling between mass and momentum transport between each phase is highly nonlinear, especially at the scale of the pore. Their investigation requires sophisticated numerical methods. Standard numerical methods include (i) pore-network models, where a simplified dynamics is solved at the scale of the pores, and (ii) macroscale (Darcy-scale) models of multiphase transport where the dynamics at the pore scale is averaged in terms of simple constitutive equations. We remark that both methods offer several advantages in terms of computational simplicity and possibility of investigating larger sample volumes. However, a proper account of reactive transport and its effect on the flow transport requires a more complex approach, where conservation equations are actually solved at the pore scale (Woods & Farcas 2009).

In this study, we present a new numerical approach for multiphase reactive flows in porous media at the pore scale, where the pore geometry can be arbitrarily complex. We use the numerical model to investigate (i) the effect of the reaction on non-wetting fluid flow pathways (capillary channels), (ii) the importance of the injection rate of the buoyant non-wetting fluid carrying the reactant, and (iii) the penetration depth of

reactant advected beyond the diffusing reaction front. We compare our results with scaling laws obtained for simple geometries in the limit of low reaction rates and observe good agreement between the two. Our calculations show that (i) capillary channels are not stable when the reaction rate is large (when the flow pathways are evolving rapidly because of melting/dissolution), (ii) in the limit of small St, the radial transport of reactant out of the capillary channel decays exponentially with the depth of penetration in the porous medium, and (iii) the aspect ratio of isocontours of reactant concentration in the non-wetting fluid channels scales like the local Péclet number.

This study allows us to better understand the evolution of the spatial and temporal distribution of each fluid phase and reactant in porous media during dissolution/melting and using different injection rates of non-wetting fluid. However, a significant amount of work is required to incorporate the small-scale physics learned from realistic pore-scale calculation into field-scale models. We believe that the challenges associated with the development of detailed pore-scale models and their upscaling is a difficult but necessary step towards a better understanding of reactive transport.

A.P. and C.H. would like to thank the Swiss National fund for a graduate student fellowship (200021-11635911) and a postdoctoral fellowship (PBSKP2-128477) respectively. O.B. acknowledges funding from the US NSF grant NSF-EAR 0809828 and B.C. the Swiss National Foundation. The authors are thankful to J. Latt and O. Malaspinas for advice and constant support. Moreover, the authors acknowledge CADMOS for giving access to its IBM Blue Gene P. Finally, the authors thank Dr Lohse for the careful editorial handling and three anonymous reviewers who helped us improve the manuscript.

REFERENCES

ANDERSON, D. M, MCFADDEN, G. B. & WHEELER, A. A. 1998 Diffuse-interface methods in fluid mechanics. *Annu. Rev. Fluid Mech.* **30**, 139–165.

AUZERAIS, F. M., DUNSMUIR, J., FERRÉOL, B. B., MARTYS, N., OLSON, J., RAMAKRISHNAN, T. S., ROTHMAN, D. H. & SCHWARTZ, L. M. 1996 Transport in sandstone: a study based on three dimensional microtomography. *Geophys. Res. Lett.* **23** (7), 705–708.

AVRAMI, M. 1940 Kinetics of phase change. *Intl J. Chem. Phys.* **8**, 212–224.

BACHMANN, O. & BERGANTZ, G. W. 2006 Gas percolation in upper-crustal silicic crystal mushes as a mechanism for upward heat advection and rejuvenation of near-solidus magma bodies. *J. Volcanol. Geotherm. Res.* **149**, 85–102.

BEJAN, A. 2004 *Convection Heat Transfer*. Wiley.

BÉNARD, C., GOBIN, D. & MARTINEZ, F. 2006 Melting in rectangular enclosures: experiments and numerical simulations. *J. Heat Transfer* **107**, 794–803.

BERTRAND, O., BINET, B., COMBEAU, H., COUTURIER, S., DELANNOY, Y., GOBIN, D., LACROIX, M., LE QUÉRÉ, P., MÉDALE, M., MENCINGER, J., SADAT, H. & VIEIRA, G. 1999 Melting driven by natural convection. A comparison exercise: first results. *Intl J. Therm. Sci.* **38**, 5–26.

BHATNAGAR, P. L., GROSS, E. P. & KROOK, M. 1954 A model for collision processes in gases. Part I. Small amplitude processes in charged and neutral one-component systems. *Phys. Rev.* **94**, 511–525.

BLUNT, M. J. 2001 Flow in porous media pore network models and multiphase flow. *Curr. Opin. Colloid Interface Sci.* **6**, 197–207.

BOEK, E. S. & VENTUROLI, M. 2010 Lattice Boltzmann studies of fluid flow in porous media with realistic rock geometries. *Comput. Math. Appl.* **7**, 2305–2314.

CAHN, W. & HILLIARD, J. E. 1958 Free energy of a nonuniform system. Part I. Interfacial energy. *J. Chem. Phys.* **28**, 258.

CARSLAW, H. S. & JAGER, J. C. 1959 *Conduction of Heat in Solids*, 2nd edn. Oxford Science Publications.

CHAPWANYA, M. & STOCKIE, J. M. 2010 Numerical simulations of gravity-driven fingering in unsaturated porous media using a non-equilibrium model. *Water Resour.* **46**, W09534.

CHEN, S. & DOOLEN, G. D. 1998 Lattice Boltzmann method for fluid flows. *Annu. Rev. Fluid Mech.* **30**, 320–364.

CHEN, Y. J. & STEEN, P. H. 1997 Dynamics of inviscid capillary breakup: collapse and pinchoff of a film bridge. *J. Fluid Mech.* **341**, 245–267.

CHIN, J., BOEK, E. S. & COVENEY, P. V. 2002 Lattice Boltzmann simulation of the flow of binary immiscible fluids with different viscosities using the Shan–Chen microscopic interaction model. *Phil. Trans. R. Soc. Lond.* A **360**, 547–558.

CHOPARD, B., FALCONE, J. & LATT, J. 2009 The lattice Boltzmann advection–diffusion model revisited. *Eur. J. Phys.* **171**, 245–249.

COLES, M. E., MUEGGE, R. D., JONES, K. W., DOWD, B., SIDDONS, B., PESKIN, P., BROOKHAVEN, A. & SPANNE, P. 1998 Developments in synchrotron X-ray microtomography with applications to flow in porous media. *SPE Annual Technical Conference and Exhibition, SPE Res. Engng* **1**, 288–296.

CUETO-FELGUEROSO, L. & JUANES, R. 2008 Nonlocal interface dynamics and pattern formation in gravity-driven unsaturated flow through porous media. *Phys. Rev. Lett.* **101**, 244504.

CUETO-FELGUEROSO, L. & JUANES, R. 2009*a* Stability analysis of a phase-field model of gravity-driven unsaturated flow through porous media. *Phys. Rev.* E **79**, 036301.

CUETO-FELGUEROSO, L. & JUANES, R. 2009*b* A phase-field model of unsaturated flow. *Water Resour. Res.* **45**, W10409.

DAY, R. F., HINCH, E. J. & LISTER, J. R. 1998 Self-similar capillary pinchoff of an inviscid fluid. *Phys. Rev. Lett.* **80**, 704–707.

VAN DUIJN, C., PIETERS, G. & RAATS, P. 2004 Steady flows in unsaturated soils are stable. *Transp. Porous Med.* **57**, 215–244.

EGGERS, J. 1993 Universal pinching of 3D axisymmetric free surface flow. *Phys. Rev. Lett.* **71**, 3458.

EGOROV, A., NIEBER, R., DAUTOVAND, J. & SHESHUKOV, A. 2003 Stability analysis of gravity driven infiltration flow. *Water Resour. Res.* **39** (9), 1266.

ELIASSI, M. & GLASS, R. 2001 On the continuum scale modelling of gravity driven fingers in unsaturated porous media: the inadequacy of the Richards equation with standard monotonic constitutive relations and hysteretic equations of state. *Water Resour. Res.* **37** (8), 2019–2035.

EWING, R. P. & BERKOWITZ, B. 1998 A generalized growth model for simulating initial migration of dense non-aqueous phase liquids. *Water Resour. Res.* **34**, 611–622.

FARCAS, A. & WOODS, A. W. 2009 The effect of drainage on the capillary retention of CO_2 in a layered permeable rock. *J. Fluid Mech.* **618**, 349–359.

FÜRST, T., VODÁK, R., ŠIR, M. & BÍL, M. 2009 On the incompatibility of Richards' equation and finger-like infiltration in unsaturated homogeneous porous media. *Water Resour. Res.* **45**, W03408.

GINGOLD, R. A. & MONAGHAN, J. J. 1977 Smoothed particle hydrodynamics: theory and application to non-spherical stars. *Mon. Not. R. Astron. Soc.* **181**, 375–389.

GLASS, R. J., STEENHUIS, T. & PARLANGE, J.-Y. 1989 Wetting front instability. Part 2. Experimental determination of relationships between system parameters and two-dimensional unstable flow field behavior in initially dry porous media. *Water Resour. Res.* **25**, 1195–1207.

GROSFILS, P., BOON, J. P., CHIN, J. & BOEK, E. S. 2004 Structural and dynamical characterization of Hele–Shaw viscous fingering. *Phil. Trans. R. Soc. Lond.* A **362**, 1723–1734.

GUNSTENSEN, A. K., ROTHMAN, D. H., ZALESKI, S. & ZANETTI, G. 1991 Lattice Boltzmann model for immiscible fluid. *Phys. Rev.* A **43**, 4320.

GUO, Z., SHI, B. & ZHENG, C. 2002*a* A coupled lattice BGK model for the Boussinesq equations. *Intl J. Numer. Meth.* **39**, 325–342.

GUO, Z., ZHENG, C. & SHI, B. 2002*b* Discrete lattice effects on the forcing term in the lattice Boltzmann method. *Phys. Rev.* E **65**, 046308.

HAGEDORN, J. G., MARTYS, N. S. & DOUGLAS, J. F. 2004 Breakup of a fluid thread in a confined geometry: droplet-plug transition, perturbation sensitivity, and kinetic stabilization with confinement. *Phys. Rev.* E **69**, 056312.

HE, X., CHEN, S. & ZHANG, R. 1999 A lattice Boltzmann scheme for incompressible multiphase flow and its application in simulation of Rayleigh–Taylor instability. *J. Comput. Phys.* **152**, 642–663.

HERSUM, T. G. & MARSH, B. D. I. 2006 Igneous microstructures from kinetic models of crystallization. *J. Volcanol. Geotherm. Res.* **154**, 34–47.

HIRT, C. W. & NICHOLS, B. D. 1981 Volume of fluid (VOF) method for the dynamics of free boundaries. *J. Comput. Phys.* **39**, 201.

HOMSY, G. M. 1987 Viscous fingering in porous media. *Annu. Rev. Fluid Mech.* **19**, 271–311.

HOOGERBRUGGE, P. J. & KOELMAN, J. M. V. A. 1992 Simulating microscopic hydrodynamic phenomena with dissipative particle dynamics. *Europhys. Lett.* **19**, 155–160.

HUANG, H., MEAKIN, P. & LIU, M. 2005 Computer simulation of two-phase immiscible fluid motion in unsaturated complex fractures using a volume of fluid method. *Water Resour. Res.* **41**, W12413.

HUANG, H., THORNE, D. T., SCHAAP, M. G. & SUKOP, M. C. 2007 Proposed approximation for contact angles in Shan-and-Chen-type multicomponent multiphase lattice Boltzmann models. *Phy. Rev.* E **76**, 066701.

HUBER, C., BACHMANN, O. & MANGA, M. 2010 Two competing effects of volatiles on heat transfer in crystal-rich magmas: thermal insulation vs defrosting. *J. Petrol.* **51**, 847–867.

HUBER, C., PARMIGIANI, A., CHOPARD, B., MANGA, M. & BACHMANN, O. 2008 Lattice Boltzmann model for melting with natural convection. *Intl J. Heat Fluid Flow* **29**, 1469–1480.

HUPPERT, H. E. 1982 Flow and instability of a viscous current down a slope. *Nature* **300**, 427–429.

JANY, P. & BEJAN, A. 1988 Scaling theory of melting with natural convection in an enclosure. *Intl J. Heat Mass Transfer* **31**, 1221–1235.

JIAUNG, W. S., HO, J. R. & KUO, C. P. 2001 Lattice Boltzmann method for the heat conduction problem with phase change. *Numer. Heat Transfer* **39**, 167–187.

KANG, Q., LICHTNER, P. C. & ZHANG, D. 2006 Lattice Boltzmann pore-scale model for multicomponent reactive transport in porous media. *J. Geophys. Res.* **111**, B05203.

KANG, Q. J., ZHANG, D. X. & CHEN, S. Y. 2005 Displacement of a three-dimensional immiscible droplet in a duct. *J. Fluid Mech.* **55**, 41–66.

LATT, J., COURBEBAISSE, G., CHOPARD, B. & FALCONE, J. L. 2004 Lattice Boltzmann modeling of injection moulding process. In *Cellular Automata for Research and Industry* (ed. P. M. A. Sloot, B. Chopard & A. G. Hoekstra). pp. 345–354. Springer.

LATT, J., MALASPINAS, O. & CHOPARD, B. 2010 External force and boundary conditions in lattice Boltzmann. *Phys. Rev.* E (submitted).

LENORMAND, R., TOUBOUL, E. & ZARCONE, C. 1988 Numerical models and experiments on immiscible displacements in porous media. *J. Fluid Mech.* **189**, 165–187.

LUNDEGARD, P. D. & ANDERSEN, G. 1996 Multiphase numerical simulation of air sparging performance. *Ground Water* **34**, 451–460.

MANGA, M. & STONE, H. A. 1993 Buoyancy-driven interactions between deformable drops at low Reynolds numbers. *J. Fluid Mech.* **256**, 647–683.

MARTYS, N. & CHEN, H. 1996 Simulation of multicomponent fluids in complex three-dimensional geometries by the lattice Boltzmann method. *Phys. Rev.* E **53**, 743–750.

MEAKIN, P. & TARTAKOVSKY, M. A. 2009 Modeling and simulation of pore-scale multiphase fluid flow and reactive transport in fractured and porous media. *Rev. Geophys.* **47**, RG3002.

NAGATSU, Y., KONDO, Y., KATO, Y. & TADA, Y. 2009 Effects of moderate Damköhler number on miscible viscous fingering involving viscosity decrease due to a chemical reaction. *J. Fluid Mech.* **625**, 97.

NAGATSU, Y., KONDO, Y., KATO, Y. & TADA, Y. 2011 Miscible viscous fingering involving viscosity increase by chemical reaction with moderate Damköhler number. *Phys. Fluids* **23**, 014109.

NAGATSU, Y., MATSUDA, K., KATO, Y. & TADA, Y. 2007 Experimental study on miscible viscous fingering involving viscosity changes induced by variations in chemical species concentrations due to chemical reactions. *J. Fluid Mech.* **571**, 475.

NEWHOUSE, L. A. & POZRIKIDIS, C. 1992 The capillary instability of annular layers and liquid threads. *J. Fluid Mech.* **242**, 193–209.

NIEBER, J., DAUTOV, R., EGOROV, A. & SHESHUKOV, A. 2005 Dynamic capillary pressure mechanism for instability in gravity-driven flow: review and extension to very dry conditions. *Transp. Porous Med.* **58**, 147–172.

NIEBER, J., SHESHUKOV, A., EGOROV, A. & DAUTOV, R. 2003 Non-equilibrium model for gravity-driven fingering in water repellent soils: formulation and 2-D simulations. In *Soil Water Repellency: Occurrence, Consequences and Amelioration*, pp. 245–258. Elsevier.

OLSON, J. F. & ROTHMAN, D. H. 1997 Two-fluid flow in sedimentary rock: simulation, transport and complexity. *J. Fluid Mech.* **17**, 181–196.

OSHER, S. & SETHIAN, J. A. 1988 Fronts propagating with curvature-dependent speed: algorithms based on Hamilton–Jacobi formulations. *J. Comput. Phys.* **79**, 12–49.

PALABOS, 2010 The Palabos software project http://www.palabos.org.

PAN, C., HILPERT, M. & MILLER, C. T. 2007 Lattice-Boltzmann simulation of two-phase flow in porous media. *Water Resour. Res.* **40**, W01501.

PAPAGEORGIOU, D. T. 1995 On the breakup of viscous liquid threads. *Phys. Fluids* **7**, 1529–1544.

PARMIGIANI, A., HUBER, C., CHOPARD, B., LATT, J. & BACHMANN, O. 2009 Application of the multi distribution function lattice Boltzmann approach to thermal flows. *Eur. J. Phys.* **171**, 37–43.

PATANKAR, S. V. 1980 *Numerical Heat Transfer and Fluid Flow*.

POZRIKIDIS, C. Cambridge University Press 1992 *Boundary Integral and Singularity Methods for Linearized Viscous Flow*, 2nd edn.

QUAN, S. & HUA, J. 2008 Numerical studies of bubble necking in viscous liquids. *Phys. Rev.* E **77**, 11.

SAFFMAN, P. G. & TAYLOR, G. I. 1958 The penetration of a fluid into a porous medium or Hele–Shaw cell containing a more viscous fluid. *Annu. Rev. Fluid Mech.* **19**, 271–314.

SCHAAP, M. G., PORTER, M. L., CHRISTENSEN, B. S. & WILDENSCHILD, D. 2007 Comparison of pressure-saturation characteristics derived from computed tomography and lattice Boltzmann simulations. *Water Resour. Res.* **43**, W12S06.

SHAN, X. 1997 Simulation of Rayleigh–Bénard convection using a lattice Boltzmann method. *Phys. Rev.* E **55**, 2780–2788.

SHAN, X. & CHEN, H. 1993 Lattice Boltzmann model for simulation flows with multiple phases and components. *Phys. Rev.* E **47**, 1815.

SHAN, X. & DOOLEN, G. D. 1995 Multicomponent lattice Boltzmann model with interparticle interaction. *J. Stat. Phys.* **81**, 379.

SIEROU, A. & LISTER, J. R. 2003 Self-similar solutions for viscous capillary pinch-off. *J. Fluid Mech.* **497**, 381–403.

STONE, H. A. & LEAL, L. G. 1990 The effects of surfactants on drop deformation and breakup. *J. Fluid Mech.* **220**, 161–186.

SUKOP, M. C., HUANG, H., LIN, C. L., DEO, M. D., KYEONGSEOK, O. H. & MILLER, J. D. 2008 Distribution of multiphase fluids in porous media: comparison between lattice Boltzmann modeling and micro-X-ray tomography. *Phy. Rev.* E **77**, 026710.

SUKOP, M. C. & OR, D. 2003 Invasion percolation of single component, multiphase fluids with lattice Boltzmann models. *Physica* B **338**, 298–303.

SWIFT, M., ORLANDINI, S., OSBORN, W. & YEOMANS, J. 1996 Lattice Boltzmann simulation of liquid–gas and binary-fluid system. *Phys. Rev.* E **54**, 5041.

TOMOTIKA, S. 1935 On the instability of a cylindrical thread of a viscous liquid surrounded by another viscous fluid. *Proc R. Soc. Lond. Ser.* A **150** (870), 322–337.

WOODS, A. W. & FARCAS, A. 2009 Capillary entry pressure and the leakage of gravity currents through a sloping layered permeable rock. *J. Fluid Mech.* **618**, 361–379.

WOODS, A. W. & NORRIS, S. 2010 On the role of caprock and fracture zones in dispersing gas plumes in the subsurface. *Water Resour. Res.* **46**, W08522.

ZHANG, W. W. & LISTER, J. R. 1999 Similarity solutions for capillary pinch-off in fluids of different viscosity. *Phys. Rev. Lett.* **83**, 1151–1154.

ZOU, Q. & HE, X. 1997 On pressure and velocity boundary conditions for the lattice Boltzmann BGK model. *Phys. Fluids* **9** (6), 1591–1598.